UC San Diego
UC San Diego Electronic Theses and Dissertations

Title
Super-Resolution Imaging by Metamaterial-Assisted Illumination

Permalink
https://escholarship.org/uc/item/81w0w64w

Author
Ma, Qian

Publication Date
2018

Peer reviewed|Thesis/dissertation

UNIVERSITY OF CALIFORNIA SAN DIEGO

Super-Resolution Imaging by Metamaterial-Assisted Illumination

A dissertation submitted in partial satisfaction
of the requirements for the degree
Doctor of Philosophy

in

Electrical Engineering (Photonics)

by

Qian Ma

Committee in charge:

> Professor Zhaowei Liu, Chair
> Professor Sadik C. Esener
> Professor Ratneshwar Lal
> Professor Yu-Hwa Lo
> Professor Donald J. Sirbuly

2018

The Dissertation of Qian Ma is approved, and it is acceptable in quality and form for publication on microfilm and electronically:

_____

_____

_____

_____

Chair

University of California San Diego

2018

EPIGRAPH

There is nothing so small*, as to escape our inquiry.*

—Robert Hooke

TABLE OF CONTENTS

LIST OF FIGURES

ACKNOWLEDGEMENTS

I would like to express my sincere gratitude to my advisor, Prof. Zhaowei Liu for his continuous support of my Ph.D. study. He brought me into the research field of optical imaging and taught me the qualities required to be a good researcher. His guidance helped me in all the time of research, from defining problems, conducting experiments to making presentations. His insightful advices on both research as well as on my career have been invaluable.

I would also like to thank my committee members, Prof. Yu-Hwa Lo, Prof. Sadik C. Esener, Prof. Ratneshwar Lal and Prof. Donald J. Sirbuly. I am grateful that they share their knowledge and experiences with me and guide me during the pursuit of my Ph.D. degree.

My labmates and collaborators are warmly thanked for their assistance on the projects. In particular, I would like to thank Dr. Anna Bezryadina, Dr. Eric Huang and Junxiang Zhao for forming such a supportive team environment for the super-resolution imaging project and Dr. Feifei Wei, Dr. Dylan Lu, and Dr. Hao Shen for training me on lab skills and helping me with projects in the beginning years of my Ph.D. program.

Finally, I want to thank my family and friends, for being supportive throughout the good times and bad times in graduate school; I could not have done it without them.

Chapter 2, in part, is a reprint of the material as it appears in National Science Reviews, 2017, nwx152. Q. Ma, Z. Liu, "Metamaterial-assisted illumination nanoscopy". The dissertation author was the first author of this paper.

Chapter 2, in part, is a reprint of the material as it appears in Nanoscale, 2017, 9, 18268-18274. Q. Ma, H. Hu, E. Huang, and Z. Liu, "Super-resolution imaging by

metamaterial-based compressive spatial-spectral transformation". The dissertation author was the first author of this paper.

Chapter 3, in part, has been submitted for publication of the material as it may appear in Nature Communications, 2018. Q. Ma, H. Qian, S. Montoya, W. Bao, L. Ferrari, H. Hu, E. Khan, Y. Wang, E. Fullerton, E. Narimanov, X. Zhang, Z. Liu, "Experimental demonstration of hyperbolic metamaterial assisted illumination nanoscopy". The dissertation author was the first author of this paper.

Chapter 4, in part, is currently being prepared for submission for publication of the material. Q. Ma, L. Khorashad, J. Zhao, Z. Liu. "Metamaterial-assisted speckle illumination microscope". The dissertation author was the first author of this paper.

VITA

2012	Bachelor of Engineering, Zhejiang University, China
2014	Master of Science, University of California San Diego
2014-2018	Graduate Student Researcher, University of California San Diego
2018	Doctor of Philosophy, University of California San Diego

PUBLICATIONS

Q. Ma, Z. Liu, "Metamaterial-Assisted Illumination Nanoscopy", National Science Review, nwx152 (2017)

Q. Ma, H. Hu, E. Huang, and Z. Liu, "Super-resolution imaging by metamaterial-based compressive spatial-spectral transformation," Nanoscale, 2017,9,18268-18274 (2017)

Q. Ma, B. Khademhosseinieh, E. Huang, H. Qian, M. A. Bakowski, E. R. Troemel, and Z. Liu, "Three-dimensional fluorescent microscopy via simultaneous illumination and detection at multiple planes," Sci. Rep. 6, 31445 (2016)

E. Huang, **Q. Ma**, and Z. Liu, "Ultrafast Imaging using Spectral Resonance Modulation.," Sci. Rep. 6, 25240 (2016).

E. Huang, **Q. Ma**, and Z. Liu, "Etalon Array Reconstructive Spectrometry," Sci. Rep. 7, 40693 (2017).

 J. L. Ponsetto, A. Bezryadina, F. Wei, K. Onishi, H. Shen, E. Huang, L. Ferrari, **Q. Ma**, Y. Zou, and Z. Liu, "Experimental Demonstration of Localized Plasmonic Structured Illumination Microscopy," ACS Nano 11, 5344-5350 (2017).

Q. Ma, H. Hu, E. Huang, and Z. Liu, "Metamaterial based compressive spatial-spectral transformation microscope," in Conference on Lasers and Electro-Optics (2017).

Q. Ma, H. Qian, S. Montoya, W. Bao, L. Ferrari, H. Hu, E. Khan, Y. Wang, E. Fullerton, E. Narimanov, X. Zhang, Z. Liu, "Experimental demonstration of hyperbolic metamaterial assisted illumination nanoscopy," manuscript in preparation

Q. Ma, L. Khorashad, J. Zhao, Z. Liu. "Metamaterial-assisted speckle illumination microscope," manuscript in preparation

FIELD OF STUDY

Major Field: Electrical Engineering

Studies in Electrical Engineering (Photonics)

Professor Zhaowei Liu

ABSTRACT OF THE DISSERTATION

Super-Resolution Imaging by Metamaterial-Assisted Illumination

by

Qian Ma

Doctor of Philosophy in Electrical Engineering (Photonics)

University of California San Diego, 2018

Professor Zhaowei Liu, Chair

This thesis presents theoretical and experimental demonstrations of using hyperbolic metamaterial illumination to go beyond the diffraction limit of optical microscopy. This technique, named as metamaterial assisted illumination nanoscope (MAIN), combines near-field patterned illumination generated by hyperbolic metamaterials (HMM) and far-field detection of an optical microscope to achieve super-resolution. A few designs of hyperbolic metamaterial to project series of sub-wavelength patterned illumination, as well as a few optical detection configurations, are studied.

An ideal HMM that is homogenous and highly-dispersive is studied by simulation. By implementing well-designed nanostructures, the HMM is capable to project a series of near-field wavelength-dependent patterns with ultrahigh resolution. Those patterns are then

utilized to illuminating an object in a compressive sensing single pixel imager configuration in which 12 nm resolution is numerically demonstrated.

A practical HMM, consisting of composite Ag-SiO$_2$ multilayers, is studied in experiment. The dispersion property and resolution-limit of such a multilayer HMM are experimentally measured. The HMM shapes the beam into a thin line which can be scanned laterally by tuning wavelength. Proof-of-concept experiment demonstrates the super-resolution capability of MAIN. About 80 nm resolution along one dimension of a 2D image is presented.

By replacing the line-illumination to speckle-illumination at near field of the HMM, Speckle-MAIN can achieve 2D super-resolution. Speckle-MAIN prototypes a super-resolution microscope down to 50 nm resolution with a metamaterial substrate and a low-cost, easy-implemented optical system.

Chapter 1

Introduction

Optical microscopy, after centuries of development, has become an essential tool to image and investigate biological molecules, pathways, and activities in microorganisms, cells, tissues and organs. The most significant drawback to classical optical microscopies is the limit to spatial resolution, i.e. how small a feature can be distinguished, which is set by the diffraction of light. In this dissertation, a novel approach that uses metamaterial is taken to push optical resolution over the diffraction barrier.

In this introduction chapter, the principle of optical imaging systems and some involved concepts will be explained at first, followed by a brief survey on the advancements in developing super-resolution microscopy. Then, an introduction to the metamaterial is included. An overview of this thesis is given at the end of this introductory.

1.1 Optical microscope and its diffraction-limit

Optical microscope, since invented at 1600s, has become an essential tool for micron and sub-micron level investigations in a wide variety of research fields ranging from fundamental science to medical and industrial applications. Allied with the fluorescent labelling techniques, fluorescent microscope allows selective visualization of specific cells or sub-cellular components, making it indispensable in biological laboratory. At the same time, the smaller people can see, the smaller people desire to see. Although

people are eager for such a tool to observe the infinitely small, the optical microscope helps only to the extent of its resolution—known as the diffraction limit, which is limited by the wave nature of light.

1.1.1 Propagating wave and evanescent wave

Optical microscope is essentially an optical system that collects and manipulates the propagation of light from an object to offer a magnified virtual or real image. Therefore, for any optical system to function, the prerequisite is light propagating. Light is a transverse electromagnetic wave and its propagating nature is well described by the Maxwell equations. The waveform of a complex optical field $o(x, y)$ at the object plane can be decomposed into a series of plane waves that carries different spatial frequencies contents [1]:

$$o(x,y) = \frac{1}{2\pi} \iint_{-\infty}^{+\infty} O(k_x, k_y) e^{j(k_x x + k_y y)} dk_x dk_y, \tag{1.1}$$

where $O(k_x, k_y)$ is the Fourier transform of the object wave $o(x, y)$; k_x and k_y are spatial frequency of the original object wave $o(x, y)$. When an object is described as the above equation, one with small details and sharp edges contains more high spatial frequency terms than one with large coarse features. The plane wave with excessively high spatial frequency does not propagate in common media, such as air, water, or oil. This makes the detail captured by an optical system is never infinitesimal. The propagation condition can be made insightfully with the help of the Helmholtz equation—the time-independent form of wave equation:

$$(\nabla^2 + k_0^2)\psi(x, y, z) = 0, \tag{1.2}$$

where ∇^2 is the Laplacian, k_0 is the wavenumber, and $\psi(x, y, z)$ is the wave. A general plane wave solution to this equation is

$$\psi(x, y, z) = e^{j(k_x x + k_y y + k_z z)}, \tag{1.3}$$

when k_x, k_y, k_z follows

$$k_x^2 + k_y^2 + k_z^2 = k_0^2, \tag{1.4}$$

where $k_0 = \omega/c$ is the wavenumber in air. Note that the ω is frequency of the optical wave, and c is light speed. By substituting Eq. (1.4) into Eq. (1.3), a plane wave is described as:

$$\psi(x, y, z) = e^{j(k_x x + k_y y)} e^{jz\sqrt{k_0^2 - k_x^2 - k_y^2}}, \tag{1.5}$$

where z is the propagation distance along the optical system axis. Therefore, only when $k_x^2 + k_y^2 \leq k_0^2$, the plane wave propagates and can be detected by far-field optics. When $k_x^2 + k_y^2 > k_0^2$, the plane wave becomes

$$\psi(x, y, z) = e^{j(k_x x + k_y y)} e^{-\alpha z}, \tag{1.6}$$

where $\alpha = \sqrt{k_x^2 + k_y^2 - k_0^2}$. In other words, the plane wave becomes evanescent and its amplitude decays exponentially, so that it cannot be detected by any far-field optical component. This propagation condition sets the ultimate resolution barrier of optical microscopy, also known as diffraction limit.

1.1.2 Optical imaging system and its point spread function

The optics in an imaging system are designed to collect and project the light propagating from an object onto a detector array or screen. When describing an optical imaging system, a transfer function is usually used to specify how different spatial frequencies are handled by the system. There are two types of optical imaging systems that behave differently: coherent imaging system and incoherent imaging system. In a coherent imaging system, the object is illuminated by coherent light—laser, and its imaging operation is linear with respect to the complex optical field; whereas in an incoherent imaging system, the object is illuminated by incoherent light source—LED or lamp, or the object is self-luminous—fluorescent, and its imaging operation is linear with respect to the intensities. The linear relation between the object and the image in these two type of imaging systems can be expressed as:

$$i_m(x, y) = \iint_{-\infty}^{\infty} o(x', y') h(x - x', y - y') \, dx' dy', \tag{1.7}$$

for coherent imaging system, where $i_m(x, y)$ is the complex optical field at image plane, $o(x, y)$ is the complex field at object plane, and $h(x, y)$ is the impulse response of the system;

$$I(x, y) = \iint_{-\infty}^{\infty} O(x', y') |h(x - x', y - y')|^2 dx' dy', \tag{1.8}$$

for incoherent imaging system, where $I(x, y)$ is the intensity distribution at image plane, $O(x', y')$ is intensity distribution at object plane, and $|h(x, y)|^2 = psf(x, y)$ is the point spread function (PSF). In order to study the spatial frequency contents in both coherent and

incoherent imaging system, these relations are converted to Fourier domain. After a Fourier transform applied to both sides of Eq. (1.7) and Eq. (1.8), the equations become:

$$\mathcal{F}\{i_m(x,y)\} = \mathcal{F}\{o(x,y)\} \cdot \mathcal{F}\{h(x,y)\} = \mathcal{F}\{o(x,y)\} \cdot CTF, \qquad (1.9)$$

$$\mathcal{F}\{I(x,y)\} = \mathcal{F}\{O(x,y)\}\mathcal{F}\{psf(x,y)\} = \mathcal{F}\{O(x,y)\} \cdot OTF. \qquad (1.10)$$

Note that CTF is in short for coherent transfer function, and OTF is in short for optical transfer function. Therefore, in spatial frequency domain, CTF—Fourier transform of system impulse response—is used to describe optical behavior of the coherent imaging system, whereas OTF—Fourier transform of system PSF—is used to describe the incoherent imaging system. Because the propagation of light in free space can only carry spatial frequency smaller than diffraction limit, both CTF and OTF acts as a low-pass filter that limit the bandwidth of detected spatial frequency. Based on the mathematical relationship between system impulse response and system PSF, OTF can be calculated as the autocorrelation of CTF. Therefore, using the same optical components but with coherent or incoherent light source, OTF will have its cut-off frequency twice larger than the cut-off frequency of CTF. Though the ultimate resolution limit is determined by the propagation condition, the cut-off frequency of CTF and OTF, in practice, is set by the limited physical size of lenses and refractive index of media. The term numerical aperture (NA) describes the physical characteristics of an imaging system.

$$NA = n\sin(\theta), \qquad (1.11)$$

where θ is the maximal half-angle of the cone of light that can enter imaging system and n is the refractive index of immersion media.

1.1.3 Criteria of the resolution barrier

To quantitatively state the resolution of an imaging system, the most common way is to measure the minimum distance of two point sources that can be resolved. There are two widely used criteria to define that distance [2]: Rayleigh resolution and Abbe resolution:

$$Rayleigh\ Resolution: d = 0.61\lambda/NA, \tag{1.12}$$

$$Abbe\ Resolution: d = 0.5\lambda/NA, \tag{1.13}$$

where λ is the wavelength of light, and NA is the numerical aperture. Both of them can be used to define the lateral resolution of an image system.

1.2 Far field super-resolution techniques

Given the diffraction limit of spatial resolution, the lack of imaging evidence makes biological functions and phenomena beyond that limitation remain elusive. Fortunately, recent developments in super-resolution microscopy (SRM) [3,4] go beyond the diffraction limit and reveal the nanoscale world optically. Several SRM technologies, such as stimulated emission depletion microscopy (STED) [5–7], single molecule localization microscopy (SMLM) [8–11] and structured illumination microscopy (SIM) [12–15], are well-established and widely used to elucidate biological interactions that could not be visualized before. While the techniques of STED microscopy and SMLM rely on properties of fluorescence, either saturation or switch-on/off effects, SIM takes a more optical approach.

1.2.1 STED microscope and SMLM

STED microscopy achieves super-resolution by restricting the fluorescence emission in a sub-diffraction limited region through a stimulated emission depletion process. Two coaxially aligned laser beams—an excitation beam and a STED beam—are applied to illuminate the fluorescent specimens in a STED microscope. The excitation beam, usually focused to a Gaussian shape, excites electrons in the fluorescent molecules to its excitation state; the STED beam is formed in a donut shape overlapping with the excitation beam to deplete the excited electrons in the donut area by stimulation emission. Thus, the spontaneous emission is allowed to happen only at the center of the excitation beam. By utilizing the saturation of stimulated emission and rapid photobleaching of fluorescent probes, the resolution of STED microscopy is practically determined by the power of the depletion beam. Working in a laser-scanning confocal configuration, STED microscopy can achieve video-rate imaging, where the field of view is traded off for speed.

In order to surpass the diffraction limit, SMLM microscopy, either stochastic optical reconstruction microscopy (STORM) [9,16–18] or photoactivated localization microscopy (PALM) [11,19], performs single molecule localization of photo-switchable fluorophores. The "on/off" of those fluorophores are designed and controlled in a way that only one fluorescent probe can be turned "on" within a diffraction limited area. The location of this "on" molecule is then determined by performing a 2D Gaussian fitting. This process is repeated frame by frame till each fluorophore is accurately located. Recently, a technique called MINFLUX [20], localizing photo-switched fluorescent probe by aligning it with the dark center of a donut beam, provides a solution to high localization accuracy (around 1 nm).

Both STED microscopy and SMLM rely on utilizing fluorescence mechanism to achieve super-resolution and work with high photo dosage, where photobleaching and phototoxicity can become a significant concern. Other than the photo damage issue, the widefield temporal resolution, i.e. imaging speed, is another bottleneck of these techniques. Localization-based imaging method has inevitable measurement redundancy in order to perform complete single molecule mapping. STED microscopy as a single-point scanning method, the recording time scales linearly with the area of the field of view.

1.2.2 Structured illumination microscopy

SIM is another super-resolution technique working in wide-field configuration that allows long-term live-cell imaging with relatively low light doses applied to samples. Conventional SIM achieves super-resolution by illuminating object with two-beam inference patterns. Those patterns effectively enlarge the detection bandwidth by shifting high spatial frequency content of object to low spatial frequency so that they can pass through the low-pass filter inherent in the image formation. SIM works at the linear response region of the fluorescent molecules and has much less photon dosage (~1-100W/cm^2 [14]) than aforementioned STED microscope (1-200MW/cm^2 [4]) and SMLM (1-10kW/cm^2 [4]). In SIM, super-resolution image is reconstructed from a minimum number of camera frames (e.g. 9 frames). This property makes it stand out in high-speed [21], low phototoxicity image formations. However, the conventional SIM technique only improves the system resolution by a factor of 2. The best resolution achieved is reported at 84 nm by using a large NA oil objective lens [14].

Different from the diffraction-limited two-beam interference pattern used in the conventional SIM, many other illumination methods are implemented in recent developments of SIM [22]. For instance, by illuminating with surface plasmon wave that has much shorter wavelength [23,24], the resolution of SIM can be extended to 3 times of the diffraction limit. By illuminating objects with an array of focused laser beam, SIM is capable of confocal-like image sectioning [25].

Despite which method is used to realize the structured illumination, a SIM system can be generally described as:

$$Im(x, y) = P(x, y)O(x, y) \otimes PSF(x, y), \quad (1.14)$$

where $Im(x, y)$ is the image, $P(x, y)$ is the patterned illumination, $O(x, y)$ is the object, and $PSF(x, y)$ is the point spread function in an incoherent imaging system. The spatial resolution of a SIM system is then determined by the characteristics of both illumination P and detection PSF.

When illumination pattern is uniform, i.e. $P(x, y) = 1$, Eq. (1.14) becomes

$$Im(x, y) = O(x, y) \otimes PSF(x, y), \quad (1.15)$$

The system is actually a conventional wide-field microscope, and its resolution is only determined by the detection PSF. When illumination is a Gaussian beam and detection PSF is infinitely large, for example, $PSF(x, y) = 1$ in the case that a single pixel detector is used, image is constructed by scanning the beam point by point. Eq. (1.14) becomes

$$Im(x', y') = \int G(x - x', y - y')O(x, y) \otimes PSF(x, y)dxdy =$$
$$G(x', y') \otimes O(x', y'), \quad (1.16)$$

where $G(x,y)$ is a Gaussian function that describes the focused beam. In this case, the resolution is only determined by the size of Gaussian beam illumination. Different from the two extreme cases discussed above, i.e., the former has DC spatial frequency in illumination and the latter only detects DC components, a real SIM has high spatial frequency components in both illumination and detection. For example, the structured illumination is formed by two beam interference pattern, $P(x,y) = 1 + \cos(2\pi f_0 x)$, Eq. (1.14) becomes

$$Im(x,y) = (1 + \cos(2\pi f_0))O(x,y) \otimes PSF(x,y), \qquad (1.17)$$

and its Fourier transform is

$$\widehat{Im}(f_x,f_y) = [\hat{O}(f_x,f_y) + \hat{O}(f_x - f_0, f_y) + \hat{O}(f_x + f_0, f_y)] \cdot OTF. \qquad (1.18)$$

$Im(x,y)$ represents an image that consists of mixed frequency components of $\hat{O}(f_x,f_y)$, $\hat{O}(f_x - f_0, f_y)$ and $\hat{O}(f_x + f_0, f_y)$. While OTF determines the detected spatial frequency bandwidth, the illumination pattern shifts higher spatial frequency of the object into the detection bandwidth. In addition, the structured illumination can be an arbitrary pattern, such as laser speckles. Analytical solution of image formation is not explicit in this case, but the image $O(x,y)$ can be constructed by error reduction algorithms [26]. Despite what method is employed for illumination, detection and reconstruction in a SIM system, the resolution limit is the summation of illumination spatial frequency f_0 and the cut-off frequency of detection OTF.

1.3 Hyperbolic metamaterial for super-resolution imaging

As discussed in previous sections, a conventional optical microscope has the diffraction limit which is about one half of the wavelength of the light. While SMLM, STED microscope and SIM overcomes the diffraction limit by using either fluorescent mechanism or patterned illumination, these techniques still use diffraction-limited optical components and inevitably require trade-offs in other imaging characteristics, such as speed, phototoxicity, versatility, or field of view to reach these resolutions. In contrast to conventional diffraction-limited optics, the use of metamaterials introduces the capability to manipulate light at sub-diffraction scales. This is due to the ability for metamaterials to allow high spatial-frequency waves that are typically evanescent in air to propagate. Thus, utilizing metamaterials provides alternative strategies for super resolution imaging.

1.3.1 Hyperbolic metamaterial and its isofrequency curve

Metamaterial is an artificially engineered material that enables optical properties beyond that of any naturally occurring material. Among a variety of metamaterials, hyperbolic metamaterial [27,28] is one of the most usual classes of electromagnetic metamaterials that has distinctive properties for applications including imaging [29,30], lithography [31–33] and spontaneous emission engineering [34–36]. The concept of a material with hyperbolic behavior originates from the anisotropic permittivity tensor:
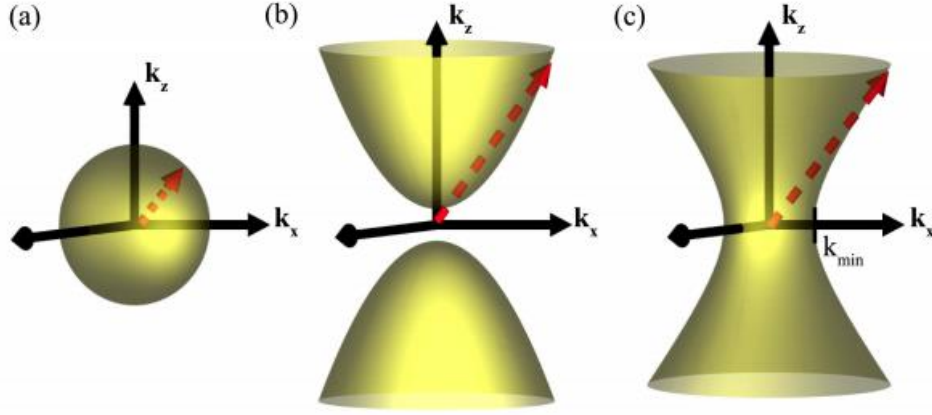
Figure 1.1: Isofrequency surface in the tridimensional k-space for (a) a conventional anisotropic medium ($\varepsilon_{xx} > 0$, $\varepsilon_{zz} > 0$) and a hyperbolic medium with (b) Type I (($\varepsilon_{xx} > 0$, $\varepsilon_{zz} < 0$) and (c) Type II ($\varepsilon_{xx} < 0$, $\varepsilon_{zz} > 0$) response. Reproduced from Ref [37].

$$\boldsymbol{\varepsilon} = \begin{bmatrix} \varepsilon_{xx} & 0 & 0 \\ 0 & \varepsilon_{yy} & 0 \\ 0 & 0 & \varepsilon_{zz} \end{bmatrix}. \tag{1.19}$$

The material is uniaxial when $\varepsilon_{xx} = \varepsilon_{yy} \neq \varepsilon_{zz}$. When transverse magnetic (TM) polarized wave propagates inside the uniaxial material, the permittivity tensor results in an anisotropic dispersion relationship among k_x, k_y and k_z:

$$\frac{k_x^2 + k_y^2}{\varepsilon_{zz}} + \frac{k_z^2}{\varepsilon_{xx}} = k_0^2. \tag{1.20}$$

When both ε_{xx} and ε_{zz} have positive sign, the material has dielectric optical properties. The isofrequency surface of k_x, k_y and k_z is ellipsoidal. When ε_{xx} and ε_{zz} has opposite signs, the isofrequency surface becomes hyperbolic, so the material is hyperbolic metamaterial. If $\varepsilon_{xx} > 0$ and $\varepsilon_{zz} < 0$, it is called Type-I hyperbolic metamaterial, and if $\varepsilon_{xx} < 0$ and $\varepsilon_{zz} > 0$, it is called Type-II hyperbolic metamaterial.

As discussed in section 1.1, a complex optical field can be decomposed into a series of plane waves with different spatial frequencies. Either Type-I or Type-II HMM supports unlimited k_x, which, in principle, means perfect resolution.

1.3.2 Hyperbolic metamaterial by composite material

In order to produce a hyperbolic metamaterial, it is essential to constrain the motion of free electrons in one or two spatial directions. This can be realized by composing metallic material (negative permittivity) and dielectric material (positive permittivity). For instance, a stack of alternating metallic and dielectric layers of deep subwavelength thicknesses, termed multilayer, has been demonstrated as an approximation of hyperbolic metamaterial. Ref [28] summaries several material combinations for fabrication of multilayer HMM that covers spectrum from ultraviolet, visible to near infrared. In visible spectrum, the multilayer HMM usually is made by silver or gold combined with a dielectric, such as Ag-SiO$_2$ [32], Ag-Si [36] and Au-Al$_2$O$_3$ [34].

The material property of the approximated HMM can be estimated by effective medium theory [38,39]:

$$\varepsilon_{xx} = p\varepsilon_m + (1-p)\varepsilon_d, \qquad (1.21)$$

$$\varepsilon_{zz} = \left(\frac{p}{\varepsilon_m} + \frac{1-p}{\varepsilon_d}\right)^{-1}, \qquad (1.22)$$

where ε_m and ε_d are the material permittivity of metal and dielectric, respectively, p is the filling ratio defined as the volume percentage of metal in a period. Despite the multilayer, other HMM material structures have also been investigated, including a 2D array of

metallic nanowires embedded in dielectric [40,41] and natural hyperbolic metamaterial [42,43].

1.3.3 Perfect lens, superlens and hyperlens

Initiated from the theoretical *perfect lens* [44], the application of metamaterial for imaging, in which the ultimate spatial frequency bandwidth is beneficial, have been studied for decades. Notable examples include superlens [45–47], hyperlens [29,48–50] and metalens [51,52]. Those metamaterial-based lens has shown promising sub-diffraction resolution [39] and cover a broad range of operation frequency [28]. The optical superlens, by using a slab of silvers, forms super-resolution image that is typically limited to the near field of the metal slab which greatly limits its application. The hyperlens, made by a hyperbolic metamaterial, introduce a magnification mechanism to send the near field images to far field so that it can be collected by an imaging sensor. This property made the hyperlens be considered as the most promising candidates for application when it was firstly invented at 2007.

Despite that, it is still challenging to apply a hyerplens in practical imaging scenario. Firstly, a hyperlens requires curved geometry to gain optical magnification, resulting in a limited field of view. Though the flat version of hyperlens is proposed based on transformation optics [53,54], the experiment has not yet demonstrated due to the complexity in fabrication. Secondly, most metamaterial at optical frequency are made by compositing dielectric and metal. Metallic losses of metamaterial-based lens require higher photon-dosage to the object to maintain reasonable signal noise ratio, which might not fit well to applications like bio-imaging.

1.4 This dissertation

This dissertation presents theoretical and experimental demonstrations of using hyperbolic metamaterial illumination to go beyond the diffraction-limit of optical microscope.

This technique, named as hyperbolic metamaterial assisted illumination nanoscope (MAIN), overcomes the aforementioned difficulties of field of view and photon-dosage in a metamaterial-based lens by ally metamaterial with structured illumination microscopy: it combines near-field high-resolution-patterned illumination generated by hyperbolic metamaterial (HMM) and far-field detection of an optical microscope to achieve super-resolution.

In chapter 2, the principle of MAIN is explained. We firstly show a homogenous HMM is capable to produce illumination patterns with resolution far beyond the diffraction-limit. Then both the method of coupling light into HMM and the method of controlling illumination patterns generated by HMM are investigated. Lastly, the homogenous HMM is implemented to make a compressive sensing single pixel imager, in which the resolution of 12 nm is theoretically demonstrated.

In chapter 3, MAIN is experimentally demonstrated. The experiment is conducted on a practical nonhomogeneous hyperbolic metamaterial which consists of composite Ag-SiO_2 multilayers. The material property is characterized, and its resolution-limit are experimentally measured. A proof-of-concept experiment of MAIN demonstrates ~80 nm resolution along one dimension of a 2D image.

In chapter 4, the methods of coupling and controlling illumination patterns are reinvestigated, providing an easy-implemented 2D super-resolution imaging solution by a

HMM-coated substrate. The refined technique, called hyperbolic metamaterial assisted speckle illumination nanoscope (speckle-MAIN), is compatible with fluorescent imaging and resolution down to 50 nm is demonstrated.

In the end, Chapter 5 discusses several future directions of MAIN and summaries this dissertation.

Chapter 2

Theory of hyperbolic metamaterial assisted illumination

In this chapter, the principle of using hyperbolic metamaterial (HMM) for illumination is introduced. A HMM illumination device can fully take advantages from HMM's wide bandwidth of spatial frequency to generate deep sub-wavelength illumination patterns. The magnification mechanism that is required in a HMM-based lens, is replaced by computational imaging method that numerically inverses the interaction between illuminating patterns and the object of interest. As an example, we demonstrate by simulation that, by arranging an array of nanoholes on an ideal, highly dispersive HMM, 12-nm imaging resolution can be achieved.

2.1 Metamaterial-assisted illumination and its advantages

Recent developments on metamaterial-based super-resolution imaging overcome that the aforementioned difficulty of lens-based approaches by merging it with structured illumination: metamaterial greatly extends the resolution and has inherent advantages from

structured illumination microscope (SIM) including high temporal resolution and low phototoxicity/photobleaching. The new metamaterials-based super-resolution imaging techniques can be generally described as metamaterial-assisted illumination nanoscopy (MAIN) and is illustrated in Figure 2.1. A piece of metamaterial is integrated into a substrate to hold objects under a widefield microscope. The metamaterial substrate (meta-substrate) shapes incident light into nanoscale structured patterns. By collecting diffraction-limited images of an object illuminated by a series of those structured patterns, MAIN can reconstruct a super-resolution images.

In SIM, the resolution is about twice of the diffraction limit of an objective lens ($\sim$ $\lambda/4$). MAIN, while its detection remains diffraction-limited, extends the resolution by projecting diffraction-unlimited illumination patterns. A meta-substrate should be designed to fulfill two major requirements for MAIN operation: firstly, it should produce deep sub-diffraction-limited light patterns; secondly, there should exist a tuning method to switch and/or shift those structured light patterns. For instance, the meta-substrate can consist of periodic plasmonic structures. This method, called Plasmonic Structured Illumination Microscopy (PSIM) excites the object by the interference patterns from two or multiple propagating surface plasmon waves and improve resolution to $\lambda/5$ [23,24]. The resolution can be further extended to $\lambda/6$ in the Localized Plasmonic Structured Illumination Microscopy (LPSIM) by introducing a meta-substrate that consists of an array of localized plasmonic resonators [55,56]. Incident angle of laser beam is used to shift the structured patterns in both cases.

To further improving the resolution, illumination patterns with even higher spatial frequency are required. HMM, supporting a wide bandwidth of spatial frequency, can

potentially improve resolution to $\lambda/40$ [39]. The beam propagation inside a HMM is studied in the following sections, and an example of MAIN is numerically demonstrated.
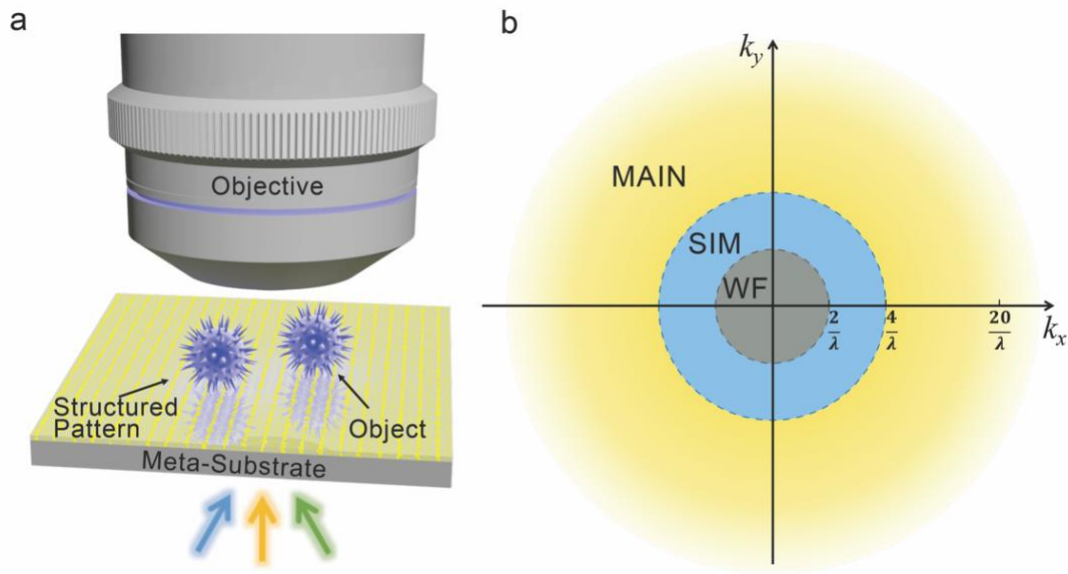
Figure 2.1: Metamaterial-assisted illumination microscope. a. Schematics of metamaterial assisted illumination nanoscopy (MAIN). A meta-substrate shapes input light into a variety of nano-scale structured patterns depending on its wavelength and/or incident angle. The object, illuminated by those patterns in series, is imaged by a diffraction-limited widefield objective. Super-resolution image of the object is numerically reconstructed afterward. b. Illustration of different imaging technologies in the spatial frequency domain (assume NA = 1). WF: widefield microscopy; SIM: structured illumination microscopy.

2.2 Propagation of light inside a hyperbolic metamaterial

Light, propagating inside a HMM, has different behavior from that in air. Firstly, infinite bandwidth of spatial frequency can be carried in an ideal HMM. Secondly, the direction of energy flow, represented by the angle of group velocity, is almost independent on the spatial frequencies, especially when k_x, or k_y is very large. While the former one enables a HMM to generate a beam in sub-diffraction-limit size, the later one ensures the beam won't diverge as it is propagating inside the HMM.

The propagating behavior of light can be derived from the hyperbolic relationship between k_x, k_y, k_z. Because x and y dimension are symmetrical, we assume k_y is zero for simplicity.

The dispersion relationship of light wave in type-II HMM follows,

$$\frac{k_x^2}{\varepsilon_z} + \frac{k_z^2}{\varepsilon_x} = \frac{\omega^2}{c^2}, \tag{2.1}$$

where $\varepsilon_z > 0, \varepsilon_x < 0$.

The HMM can be made by a stack of silver and silica thin films with silver's filling ratio 0.5. The HMM has its permittivity tensor calculated from effective medium theory. Its isofrequency curves are plotted in Fig. 2.2, showing it carries unlimited spatial frequency content.

The group velocity of beam propagating inside HMM is normal to the isofrequency wave (shown as the arrows in Fig. 2.2). When $k_x \gg k_0$,

20
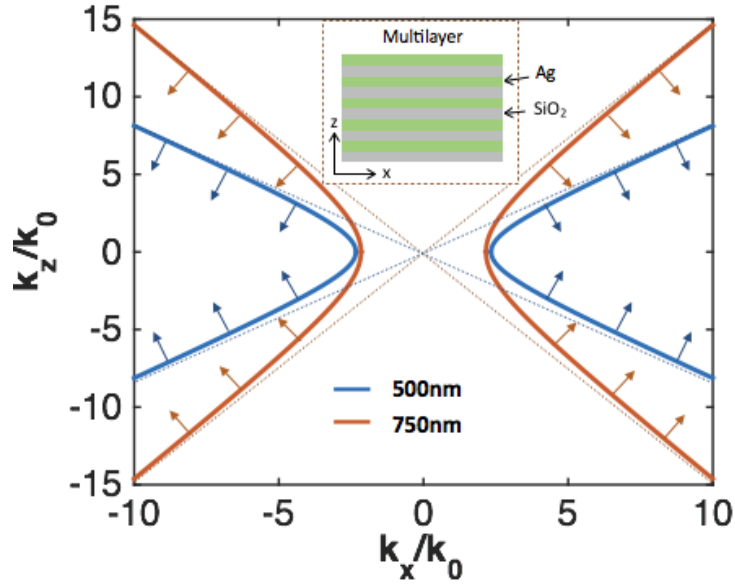
Figure 2.2: Isofrequency contours of Ag-SiO$_2$ multilayer at two wavelength 500 nm (blue) and 750 nm (red). The arrows show the direction of group velocity. Filling ratio of silver is 0.5.

$$\theta \approx \arctan\left(\sqrt{-\frac{\varepsilon_x}{\varepsilon_z}}\right),\qquad (2.2)$$

where θ is the angle between of group velocity direction and z-axis.

When a beam propagates in the air, the group velocity has the same direction with the phase velocity (direction of $\boldsymbol{k}$). As a result, a tightly focused beam that consists of a broad bandwidth of k_x will diverge when it propagates. When a beam propagates in a HMM, θ is almost independent on the spatial frequency. A focused beam won't diverge when it propagates inside the HMM. Moreover, the group velocity direction inside the HMM is wavelength-dependent so that the illuminating position can be scanned by tuning wavelength. Figure 2.2 presents two iso-frequency curves, as well as their direction of the group velocity for Ag-SiO$_2$ HMM at 500 nm and 700 nm, respectively. Figure 2.3 shows
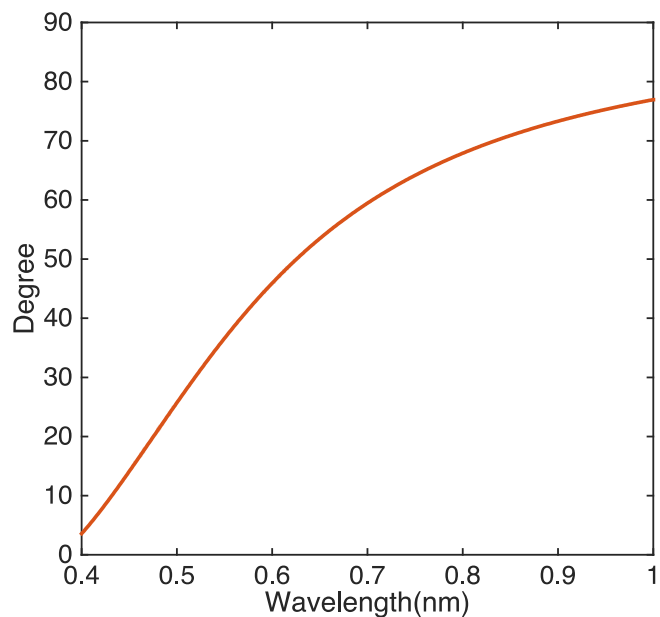
Figure 2.3: Propagating angle versus wavelength for HMM made by Ag-SiO₂ Multilayer. Permittivity of HMM is calculated by effective media theory. Filling ratio of silver is 0.5.

the calculated direction of group velocity for the whole spectrum (from 400 nm to 1000 nm).

Benefitting of the sub-diffraction beam confinement, the non-diverging propagation and the strong dispersion, when a broadband light is injected through a narrow-slit mask on one side of HMM (Figure 2.4a), the HMM, like a grating, spreads the beam based on wavelength and re-distribute them to the other side of HMM. For each wavelength, the beam remains well-confined (Figure 2.4b). Therefore, with the help of a nanoslit coupler on the bottom of HMM, a flat type-II HMM projects a nanoscale 'rainbow' on its top surface. This phenomenon is firstly applied to lithography [32], then for imaging. The imaging method of using nanoslit-coupled HMM is named as hyper-structured illumination [57,58].
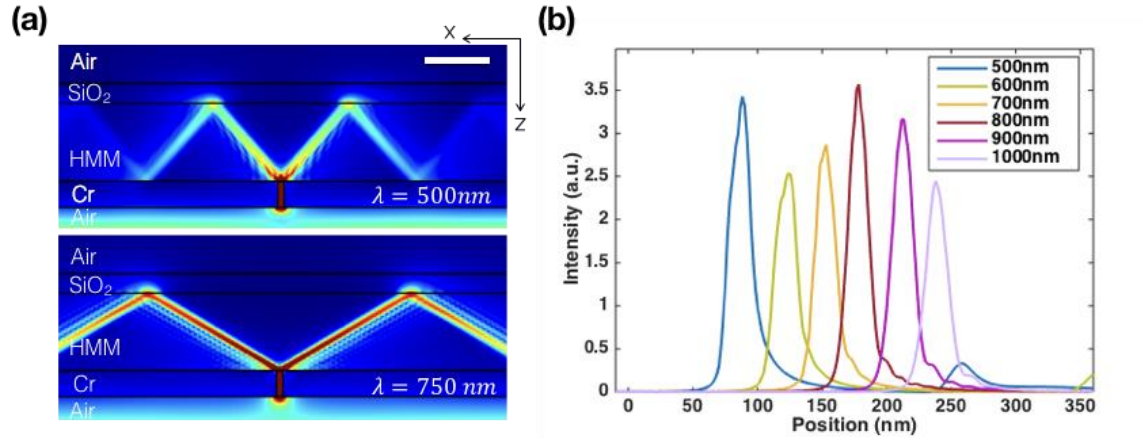
Figure 2.4: Near field illumination of nanoslit-coupled HMM. (a) Beam propagation when light coupled into HMM through a nanoslit (10 nm); a homogenous anisotropic Ag-SiO$_2$ HMM based on EMT is simulated. 10 nm air slit is opened on a 40 nm thick Cr film. (b) Illumination profile at the top of slit in-coupled HMM at a variety of wavelengths.

In the case that an object on the top of HMM is illuminated by the 'rainbow'-like beams, the imaging resolution will be mainly determined by the beam FWHM. There are three factors mainly determines the FWHM: the width of the nanoslit, the metallic loss, and the unit pair size of Ag-SiO$_2$ stacks. The width of the nanoslit determines the initial beam confinement when it in-couples from air into HMM. During beam propagation, the wave will be absorbed by the HMM due to metallic loss of silver. High spatial frequency wave gets absorbed faster than low spatial frequency waves, resulting in an enlarged beam width. With approximation of effective medium theory, the beam has FWHM ~20 nm at 500 nm wavelength when the total thickness of HMM is 130 nm. The FWHM becomes ~27 nm when HMM thickness increases to 250 nm due to material loss. Despite that, the unit cell size of the HMM also affects the FWHM, which cannot be estimated by effective medium theory (EMT). Fig. 2.5 shows the FWHM versus different sizes of HMM unit cell from full wave

23
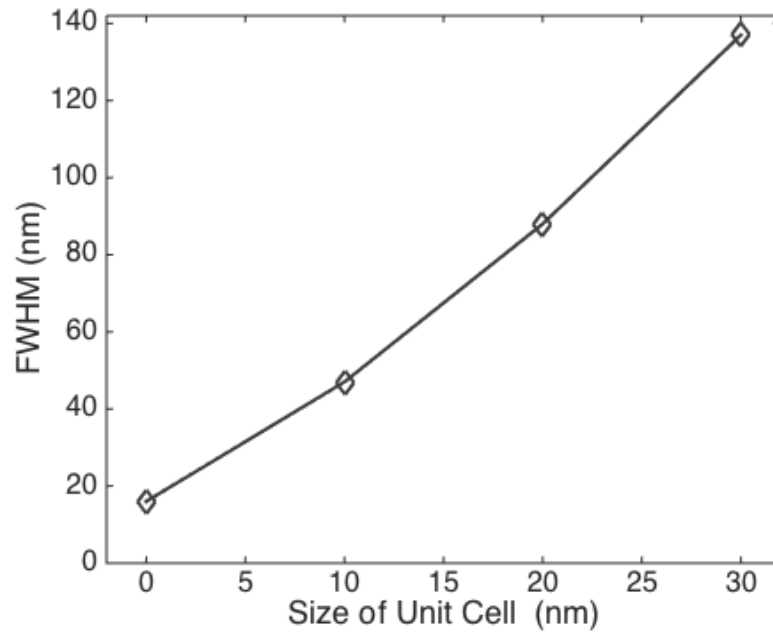
Figure 2.5: Beam width at HMM and air interface versus unit cell size of HMM. HMM consists of alternating layers of Ag and SiO_2. The filling ratio: 0.5. Total thickness of HMM: 120 nm. Unit Cell Size: 0 nm (effective medium theory), 10 nm, 20 nm and 30 nm.

simulation of a stack of silver and silica films. It requires the unit cell size of a Ag-SiO_2 multilayer to be sub-10 nm scale to have the material performance close to an ideal HMM. In following sections, EMT is used to estimate imaging performance. The effect of unit cell in a practical multilayer HMM will be discussed in Chapter 3.

2.3 Space-Spectrum Encoding

A nanoslit maps wavelength to sub-diffraction-limit spatial information along the direction that is normal the nanoslit. It is can be considered as a one-dimensional space-to-spectrum transformation, which only grants one-dimensional imaging. To achieve 2-dimensional sub-diffraction-limited image by using a planar HMM remains elusive.

Different from a nanoslit, a single nanohole on HMM bottom projects a series of concentric rings on the HMM top surface when it is illuminated by a broadband plane wave (non-polarized). The larger the wavelength, the larger radius of the ring, but with ~20 nm ring thickness (Figure 2.6) for each single wavelength. Therefore, the space-to-spectrum transformation is from one-dimensional space (ring diameter) to spectrum (wavelength). In order to get the information of the other dimension, multiple nanoholes need to be placed (~10 nm in diameter and 20 of nanoholes in this specific example) on the bottom of the HMM, as schematically sketched in Figure 2.6a. In this case, every location is encoded by a multiplexed spectrum determined by the distribution of those nanoholes.

An object is placed on the surface of HMM, which scatters the near field light into the far field. To simplify the process without losing the essence in physics, wavelength-dependence of scattering is ignored in this simulation but should be calibrated and corrected in practice (see section 2.4.4 for the cases when object wave is dispersive). The space-spectrum transformation can be generally described by:

$$S(\lambda) = \iint H(x,y,\lambda)O(x,y)dxdy, \qquad (2.3)$$
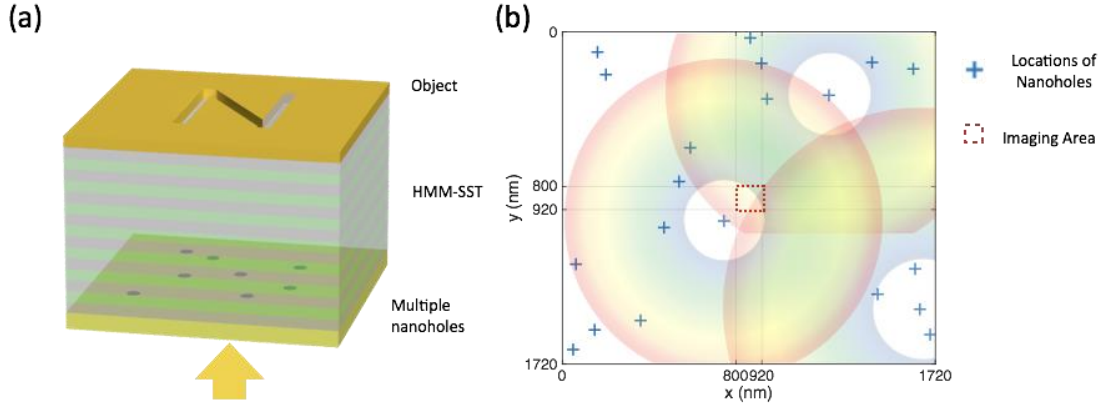
Figure 2.6: The implementation of hyperbolic metamaterial for 2D imaging. (a) Schematic of a HMM spatial-spectral transformer (SST). Multiple nanoholes are randomly distributed in a Cr photomask attached to the bottom of a HMM slab. (b) Distribution of 20 nanoholes and location of measured object area. Each nanohole forms a circular, rainbow-like illumination patterns overlapping with the object.

where S is the spectrum measured at far field, O is the object, H is a series of illumination patterns at different wavelength λ.

Equation (2.3) can be rewritten into a pixelated format,

$$S(\lambda) \approx \Delta x \Delta y \sum_{i,j=1}^{N} O(x_i, y_j) H(x_i, y_j, \lambda), \qquad (2.4)$$

where Δx, Δy are the size of pixels.

A successful image reconstruction requires each pixel in above equation has a unique encoded spectrum. To quantitatively state the maximum likelihood of encoded spectrum for any two pixels, the mutual coherence [59] of the transformation matrix H in Eq. (2.4) is calculated. The locations of those nanoholes are placed randomly, until a H with minimized mutual coherence is found (Figure 2.6b).

Figure 2.7 presents two exemplary illumination patterns (field of view: 120 nm × 120 nm) under two selected wavelengths from the transformation matrix H. Each pixel

shown in Figure 2.7b has a unique encoded spectrum from 400 nm to 1200 nm (Figure 2.7c). Since the illumination pattern is also polarization dependent, one could also add two polarization states (x-polarized and y-polarized) in the transformation to increase the total number of measurements.

By reshape $O(x_i, y_j)$ to a vector with size $N^2 \times 1$ and $H(x_i, y_j, \lambda)$ to a matrix with size $M \times N^2$, where M is the number of measurements, we can re-write the equation in a matrix multiplication form

$$I_{M \times 1} \approx H'_{M \times N^2} \cdot O_{N^2 \times 1}. \tag{2.5}$$

The effective measurements number M is limited by the number of wavelength channels that can generate distinguishable illumination patterns. M is typically smaller than N^2 in any k-space limited system. Thus, this linear equation is ill-posed and cannot be directly solved. In the following section, we use compressive sensing algorithms [60] to find a near-optimal estimation $\hat{O}$ of solution O with limited number of measurements M by assuming that the object is sparse.
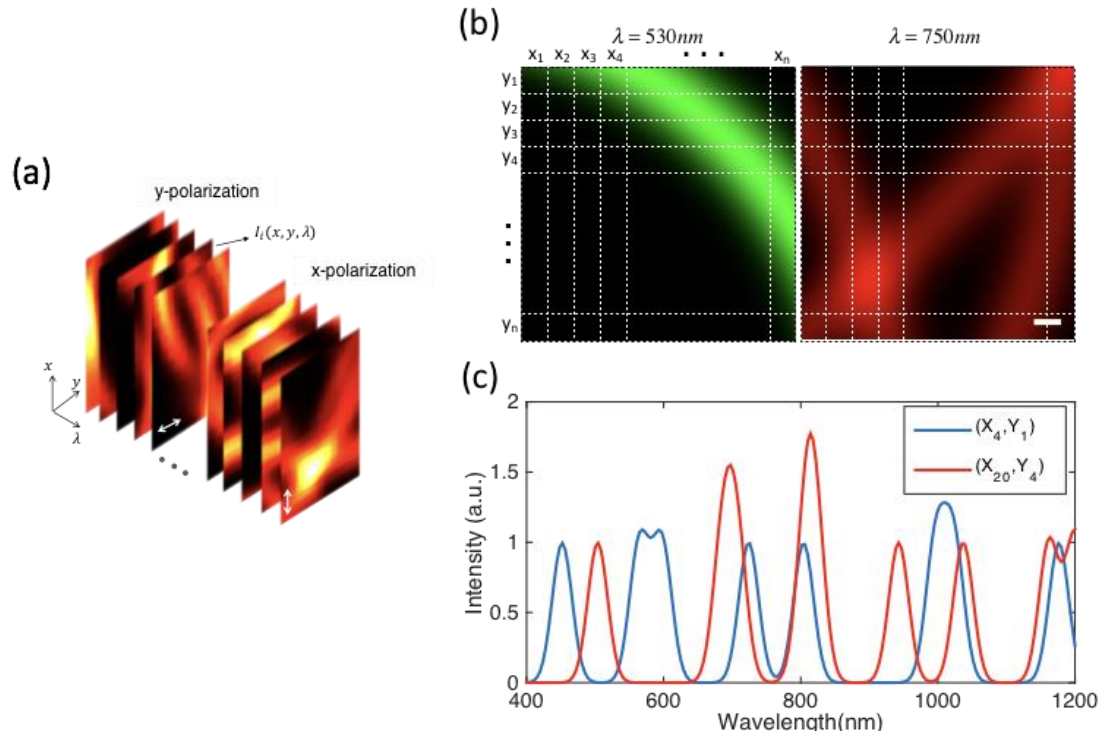
Figure 2.7: Space-spectrum encoding. (a) Transformation Matrix: stack of illumination patterns controlled by both wavelength and polarization. Wavelength: 400nm - 1200nm. Polarization: x-polarized and y-polarized. (b) Two example illumination patterns within the red dotted area in (b) generated by non-polarized light at 500nm (Left) and 750nm (Right), respectively. Scale Bar: 10 nm. (c) encoded spectrums from 400nm to 1200nm of two exemplary pixels [(X4, Y1); (X20, Y4)] in (b).

2.4 Imaging reconstruction

Compressive sensing, or compressed sensing [60], is a signal processing approach that is capable to reconstruct a signal from underdetermined linear systems, such as the system described by Eq. (2.5). The approach is based on a special constraint of the signal—the signal should be sparse in some domain. A sparse domain means that only a few percentages of elements in the domain are nonzero. The sparsity constraint can be widely adapted in imaging field because most natural images is sparse in domains such as wavelet transformation, or discrete cosine transformation [61].

A compressive sensing single pixel imager [59,62,63] is a imaging system that implements a spatial light modulator to sample an object in the compressive sampling way and mathematically reconstruct the image from much less measurements than the unknowns of the object. Allying metamaterial-shaped illumination, which can be considered as a special type of spatial light modulation, with compressive sensing enables super-resolution single pixel imager. An example of this has been demonstrated in RF frequency [64]. A super-resolution single pixel imager by hyperbolic metamaterial at optical frequency is demonstrated in the following sections.

2.4.1 l_1-regularized least squares algorithm

Reconstruct the original object requires solving an ill-posed linear inversion problem,

$$y = Ax + v,\tag{2.6}$$

where $x \in \mathbf{R}^n$ is the vector of unknowns, $y \in \mathbf{R}^m$ is the vector of measurements, $v \in \mathbf{R}^n$ is the noise and $A \in \mathbf{R}^{m \times n}$ is the transformation matrix. The number of measurements is smaller than the number of unknowns in the object.

There are infinite number of solutions to the above equation. Therefore, additional constraints of the object are required to solve the problem. The constraint used here is that the object is sparse: only a small percentage of pixels, defined as sparsity, in the objects are nonzeros. The sparsity constraint can be applied by minimizing following cost function:

$$F(x) = ||Ax - y||_2^2 + \lambda ||x||_1, \tag{2.7}$$

where $\left|\left|x\right|\right|_1$ denotes the L1 norm of x and λ is the regularization parameter. The complete reconstruction algorithm, called l1-regularized least squares, is provided in ref [65], and implemented in this research.

2.4.2 Sparsity-based image reconstruction

We firstly study the sparsity-based reconstruction under ideal condition. A pixelated binary UCSD library logo (Figure 2.8a) is sampled via a series of illumination patterns (Figure 2.9(a-f)) from 400 nm to 1200 nm with two linear polarizations (x-polarized and y-polarized plane wave). The physical size of each pixel is set to be 6 nm, smaller than half of the smallest FWHM of the illumination patterns (~27 nm). Apparently, the deep sub-wavelength object won't be directly resolved in the far field (Figure 2.9(g-i)), but the high spatial resolution information is encoded into the spectrum (Figure 2.8b). The reconstruction is done through the l1_ls algorithm. During reconstruction, we find out that if an object is known to be sparse, the reconstruction code tends to end up with a higher

resolution image compared to the illumination patterns. For instance, reconstructed result in Figure 4c can resolve two lines with 12 nm separation. We consider this as an advantage of compressive sensing, which uses a prior-knowledge of object sparsity and extrapolates the detecting bandwidth in reconstruction [66,67]. However, this phenomenon is object sparsity dependent. The working condition of sparsity-based construction, as well as reconstructed imaging resolution, should be discussed.
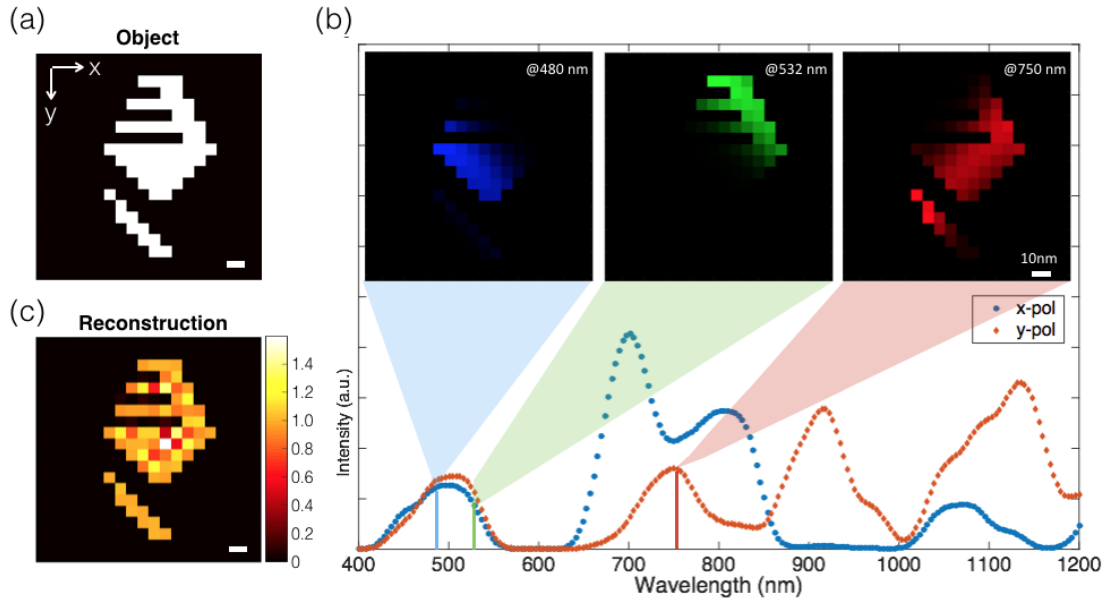
Figure 2.8: CSSTM reconstruction result under ideal conditions. (a) Test object. A simplified UCSD Logo is pixelated to 20 by 20 pixels. Physical size per pixel: 6nm. (b) Simulated spectrum in the far field under two orthogonal incident polarizations. Each data point in the spectra represents the summation of intensity at far field at a given wavelength and polarization. Three sub-images in (b) show part of object illuminated by wavelength 480 nm (x-polarization), 532 nm (x-polarization) and 750 nm (y-polarization), respectively. Spectrum has 200 wavelength channels. (c) Reconstructed image with high fidelity and resolution. Scale Bar: 10nm.
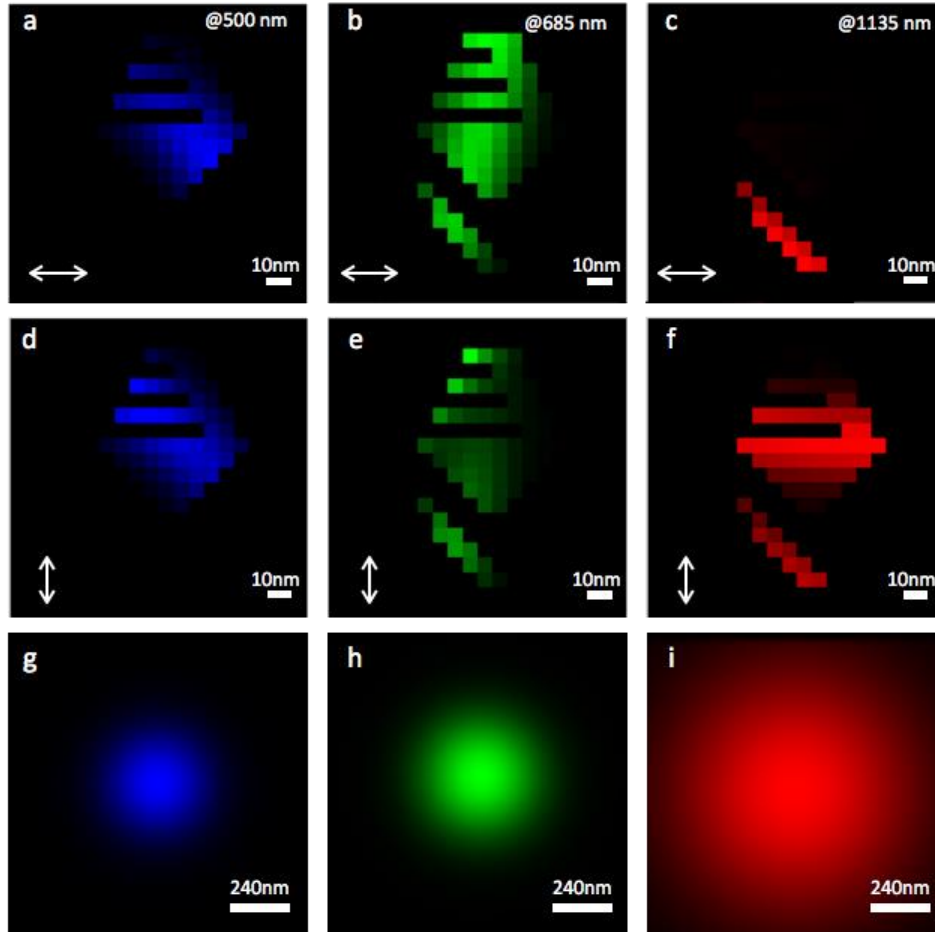
Figure 2.9: Object illuminated by different wavelengths and two polarizations. (a) Wavelength: 500nm, polarization: 0 degree. (b) Wavelength: 685nm, polarization: 0 degree. (c) Wavelength: 1135nm, polarization: 0 degree. (d) Wavelength: 500nm, polarization: 90 degree. (e) Wavelength: 685nm, polarization: 90 degree. (f) Wavelength: 1135nm, polarization: 90 degree. (g-i) Diffraction-limited image of illuminated objects under 500nm, 685nm and 1153nm, respectively (0° polarization)

2.4.3 Reconstruction accuracy

We then explore if the reconstruction is robust to noise. Because we use a sparse-based algorithm, the result also depends on the accuracy of the sparsity-constraint. Qualitatively speaking, reconstruction is more robust to noise when an object is sparse (fewer non-zero values). For instance, Figure 2.10 presents reconstruction results of two objects with different number of non-zeroes. One object only contains two non-zeros pixels (out of 400 unknowns) while the other object contains ten non-zero pixels which forms a 'smile' face. Both images are reconstructed when the SNR is 30dB. The 'smile' face starts to fail when the SNR falls to 20dB, and the 'two dots' starts to fail when the SNR is 10dB. The reconstruction accuracy is defined as

$$C = \frac{\sum_{x,y}\{Image(x,y) \cdot Object(x,y)\}}{\sum_{x,y} Image(x,y) \sum_{x,y} Object(x,y)}. \tag{2.8}$$

The reconstruction accuracy is studied numerically under different condition of object sparsity, signal noise ratio and imaging pixel size. The tuned parameters include (a) object sparsity: number of non-zeros in reconstructed imaging, ranges from 5 to 50 with a step of 2; (b) signal noise ratio: 10dB to 80dB. Step: 10dB; and (c) imaging pixel size: 6nm and 10nm. In addition, the total number of object unknowns remains the same (400 pixels).

First, an object is given as randomly switched ON (value 1) pixels on an all zeros 2D matrix. The number of ON pixels equals to the object sparsity. White Gaussian noise (given SNR) is added to the transformed spectrum measurement before reconstruction. Each data point of reconstruction accuracy is then computed through an average of 10 times (each time, both object and noise are randomly generated while SNR and Sparsity are fixed). Second, we increase the pixel size to 10 nm from 6 nm, which will increase the
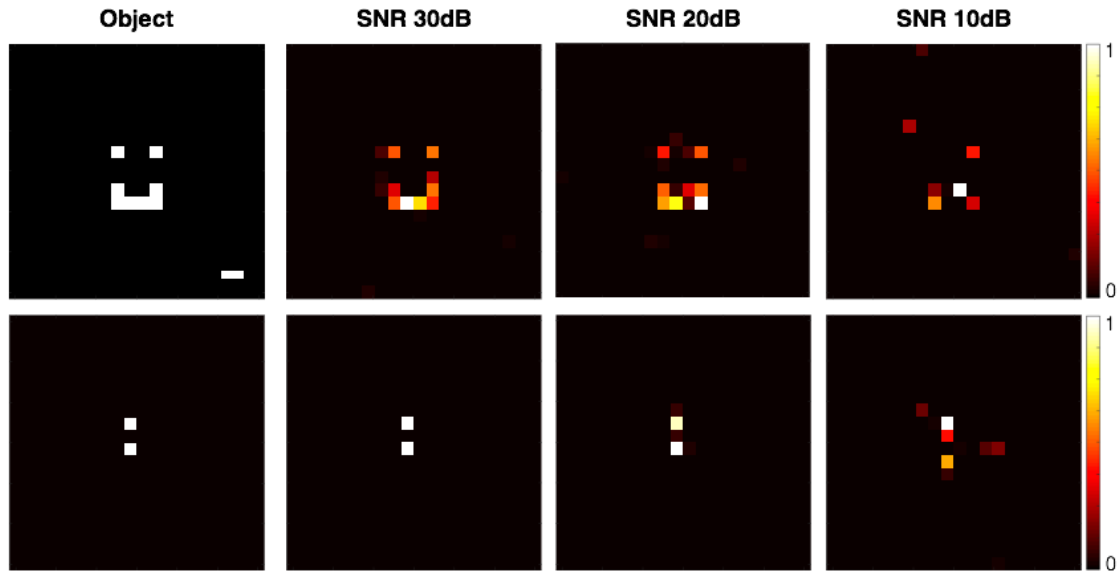
Figure 2.10: CSST reconstruction results with various noise conditions. Two objects have different sparsity conditions: The first row 'Smile Face' object and second row 'Two Dots' have 8 and 2 non-zero pixels (out of 400 total pixels), respectively. White Gaussian noise is added to the computed spectrum before reconstruction. Column 2 to 4 show reconstructed images of these two objects under different signal noise ratio [30dB, 20dB, 10dB]. Scale Bar: 10nm

contrast of encoded spectrums in adjacent pixels. The total number of object unknowns remains the same (400 pixels). Thus, image has relative lower physical resolution (20 nm) and larger field of view (200 nm × 200 nm). It is shown that increasing pixel size will either help reconstruct a less sparse object or improve reconstruction accuracy in a noisier situation. It should also be noted that increasing pixel size will give larger errors in pixelating the object and the illumination patterns. The errors are not discussed here because the pixel size is set to be ~3-4.5 times smaller than smallest feature size of illumination pattern. But the error can no longer be ignored if pixel size gets larger.
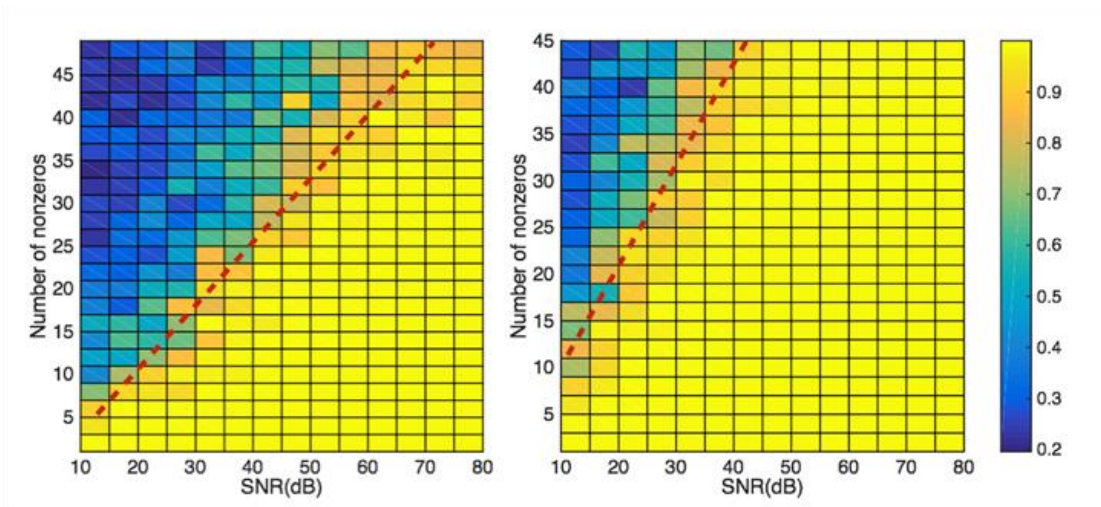
Figure 2.11: Reconstruction accuracy versus signal noise ratio and sparsity. Left: Pixel size: 6 nm. Field of View: 120 nm × 120 nm; Right: Pixel size 10 nm; Field of View: 200 nm × 200 nm. The right side of the red dashed line is considered as accurate reconstructions.

Figure 2.11 plots out reconstruction accuracy versus object sparsity and SNR. The reconstruction accuracy fails quickly when either object sparsity or SNR reaches certain barrier. If we define a threshold for reconstruction accuracy, the iso-accuracy contour in Figure 5 stands for a working window of this method.

It should be emphasized that the illumination pattern significantly affects the resolution of our imaging system. The smaller the features of the illumination patterns are, the higher resolution of the object tends to be reconstructed. In addition, our reconstruction results have higher resolution than the illumination pattern, even under a noisy signal condition. We understand this as a benefits of spatial frequency bandwidth extrapolation induced by compressive sparsity-based reconstruction. Like other extrapolation processes, whether a reconstruction will be successful is highly dependent on the noise level and the accuracy of the sparsity constraints.

Therefore, the final resolution of the CSSTM is ultimately determined by the achievable bandwidth (a half of the pixel spatial frequency of reconstructed image) with high fidelity after the reconstruction. Based on the results shown in Figure 2.9 and Figure 2.10, the resolution of CSSTM is ~2 times better than that of the illumination patterns generated by the HMM based spatial-to-spectral transformer. The trade-off between image size, sparsity of object and imaging resolution (or pixel size) are linked by the following relationship [60]:

$$M \geq C \cdot \mu^2(\mathrm{H}) \cdot S \cdot \log(n), \qquad (2.9)$$

where M is the total number of effective measurements, μ is mutual coherence of sensing matrix H in Eq. (2.5), S is the number of nonzero elements in the reconstruction basis and n is the total number of unknowns, and C is a constant.

For a given transformation mentioned above, the mutual coherence μ is related to pixel size. A large pixel size decreases the similarity of the encoded spectrum of any two adjacent pixels. Thus, it results in a smaller μ, and allows for the reconstruction of a less sparse object. However, the imaging resolution must be sacrificed accordingly. On the other hand, an increase in n means making a larger field of view without changing the pixel size, but it requires either a smaller S or a larger M for a successful reconstruction. Therefore, based on what the actual sample would be, one may need to find suitable working condition by tuning these parameters.

2.4.4 Dispersion of the object wave

Previous discussion does not consider the dispersion of object. If the scattering response of an object is wavelength dependent, the measurement equations become:

$$I(\lambda) \approx \Delta x \Delta y \sum_{i,j=1}^{N} O(x_i, y_j, \lambda) \cdot H(x_i, y_j, \lambda). \tag{2.10}$$

A completely unknown $O(x_i, y_j, \lambda)$ cannot be retrieved from above equation. Therefore, other prior-known information is required. Fortunately, in many practical situations, we do know some prior information of the object. We show two working cases here, one simplified case is that the object only consists of one type of particles, and then followed by a more complicated case that the object consists of multiple types of particles. Those cases are very similar to the case of an experimental object tagged by identical scattering particles (such as proteins, or biological organelles, or nano-spheres).

Case #1: The object is made of identical units with an unknown distribution.

In this case, $O(x_i, y_j, \lambda)$ can be simplified into two functions: object distribution function $O'(x_i, y_j)$ and response function $S(\lambda)$,

$$I(\lambda) \approx \Delta x \Delta y \sum_{i,j=1}^{N} O'^{(x_i, y_j)} \cdot S(\lambda) \cdot H(x_i, y_j, \lambda)$$

$$= \Delta x \Delta y \sum_{i,j=1}^{N} O'^{(x_i, y_j)} H'^{(x_i, y_j, \lambda)}, \tag{2.11}$$

where $S(\lambda)$ is the intensity response spectrum of a single unit. After independently measuring $S(\lambda)$, one can combine it with $H(x, y, \lambda)$ to generate a modified illumination

pattern $H'(x, y, \lambda)$. $O'(x, y)$ can then be retrieved following the same process of non-dispersive case with the modified illumination pattern.

Case #2: The object consists of more than one type of unit (assume q types of units).

$$O(x, y, \lambda) = O'_1(x, y)S_1(\lambda) + O'_2(x, y)S_2(\lambda) + \cdots O'_q(x, y)S_q(\lambda), \qquad (2.12)$$

where O'_1 to O'_q are the distribution of q types of object, respectively; S_1 to S_q are the response spectrum of q types of object, respectively.

Thus,

$$(I_\lambda)_{M \times 1}$$

$$= \begin{pmatrix} H'_{1\,M \times N^2} & H'_{2\,M \times N^2} & \cdots & H'_{q\,M \times N^2} \end{pmatrix}_{M \times (q \cdot N^2)} \begin{pmatrix} O'_{1\,N^2 \times 1} \\ O'_{2\,N^2 \times 1} \\ \vdots \\ O'_{q\,N^2 \times 1} \end{pmatrix}_{q \cdot N^2 \times 1}, \qquad (2.13)$$

where H'_1 to H'_q are the transfer matrix H modified by S_1 to S_q.

In this case, more unknown variables $\begin{pmatrix} O'_1, & O'_2, & \ldots & ,O'_q \end{pmatrix}^T$ are to be solved so that we may suffer from a low reconstruction accuracy. However, Object information O'_1 to O'_q are still retrievable, with a moderate accuracy, by applying other physical constraints to the objects $\begin{pmatrix} O'_1, & O'_2, & \ldots & ,O'_q \end{pmatrix}^T$. For example, there should be no overlaps between any two sub-objects O'_i and O'_j.

2.5 Conclusion

We explore the possibility of using HMM-generated illumination to achieve super-resolution imaging. A homogenous, highly dispersive HMM can generate a nanoscale

'rainbow' on the near field when nanostructure, either nanoslits or nanoholes is used to couple light inside HMM. Utilizing this unique phenomenon, we propose a HMM based super resolution approach, which can be named as compressive spatial-spectral transformation microscopy (CSSTM), through which super-resolution spatial information is encoded into spectral domain and then retrieved by a sparse-based reconstruction algorithm. Concept-proof simulation results are provided to demonstrate the capability of this CSSTM method. One exemplary design of the CSSTM shows successful image reconstruction with 12nm resolution and a field of view of 120 nm $\times$ 120 nm by utilizing 200 wavelength channels from 400 nm to 1200 nm. This approach is robust to noise when the object is sparse.

In contrast with other super resolution technologies, the HMM based CSSTM performs high-resolution scattering imaging based on a single shot spectrum (or two if two polarizations are used). This principle may also apply to fluorescence imaging, but it requires that the illumination spectrum can be fitted into the fluorescence absorption band. Without the cost of large numbers of measurements, we believe CSSTM is also beneficial when both temporal and spatial resolution are required.

The metamaterial utilized in this work has a flat geometry, which makes it possible to adapt wide-field imaging. However, one challenge for wide-field is to get enough measurements for the increased number of object unknowns when its field of view gets larger. One potential solution is to acquire diffraction-limited spectral images at far field. Then, each diffraction limited zone could be treated as a single-shot-spectrum imager to reconstruct high-resolution image.

Chapter 2, in part, is a reprint of the material as it appears in National Science Reviews, 2017, nwx152. Q. Ma, Z. Liu, "Metamaterial-assisted illumination nanoscopy". The dissertation author was the first author of this paper.

Chapter 2, in part, is a reprint of the material as it appears in Nanoscale, 2017, 9, 18268-18274. Q. Ma, H. Hu, E. Huang, and Z. Liu, "Super-resolution imaging by metamaterial-based compressive spatial-spectral transformation". The dissertation author was the first author of this paper.

Chapter 3

Experiment of metamaterial

assisted illumination

This chapter presents a proof-of-concept experiment on the novel illumination method based on hyperbolic metamaterial (HMM). As a demonstration example, a nanoslit-coupled HMM sample is fabricated and characterized. The space-to-spectrum transformation, as described in Chapter 2 is experimentally measured. Image resolution is demonstrated down to 80 nm and the resolution limitation is discussed.

3.1 Multilayer HMM for illumination

Optical metamaterial is capable to manipulate light in nanometer-scale that goes beyond what is possible with conventional materials. In Chapter 2, the idea of using a nanoslit-coupled HMM (or a nanohole-coupled HMM) to provide sub-diffraction-limit illumination patterns is theoretically demonstrated. Those patterns, interacting with the object of interest, transform the sub-diffraction-limit spatial information of the object to a far field spectrum. Taking advantage of this special property, metamaterial-assisted illumination nanoscopy (MAIN) possesses tremendous potential to extend the resolution far beyond the conventional structured illumination microscopy.

However, there rarely exists a natural material that has hyperbolic material property. In the range of visible wavelength, a HMM can be approximated by a metal-dielectric multilayer that is made by a stack of alternating thin metallic and dielectric films. This approximation, known as effective medium theory, is widely adapted to estimate the property of composite material when the film thickness is subwavelength, while the effective-medium theory can break down if wavelength is close the its unit thickness [39]. HMM-assisted illumination, however, relies on propagating wave with excessively large wave vectors and, hence, excessively small wavelength. Therefore, multilayer HMM behaves differently from an ideal homogenous HMM when the wavevector of propagating wave is large, causing an offset in the space-to-spectrum transformation and a decrease of imaging resolution in HMM-assisted illumination. For instance, figure 3.1 shows the beam propagation of a nanoslit-coupled HMM in which the HMM is made by Ag-SiO$_2$ multilayers (6 pairs of 10 nm Ag film and 10 nm SiO$_2$ film). Compared to the simulation of an ideal HMM (Figure 2.4), the focused beam on the HMM top surface appears to be wider, and propagation angles of the beam at plotted wavelengths are larger.

In the following sections, the space-to-spectrum transformation and imaging resolution of a nanoslit-coupled Ag-SiO$_2$ multilayer HMM are experimentally measured.
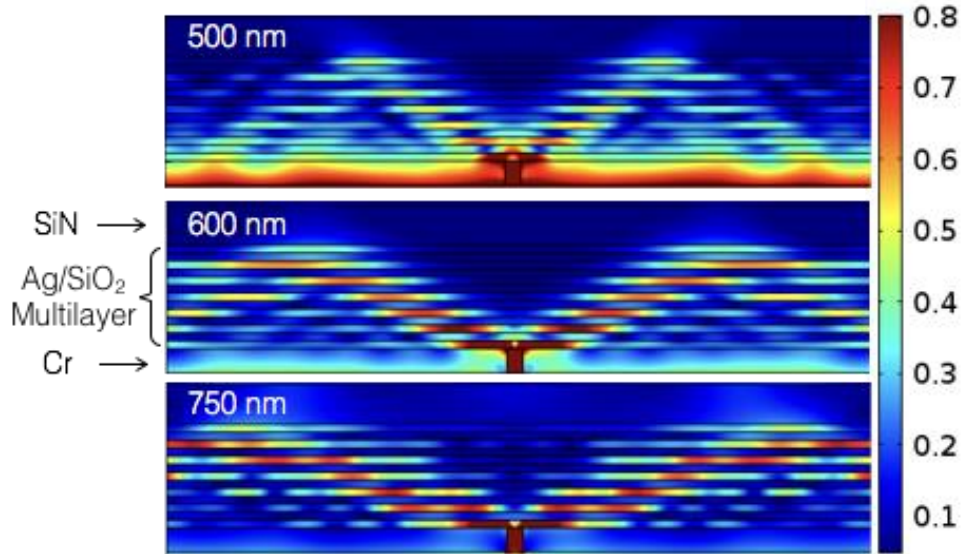
Figure 3.1: Full wave simulation of normalized electrical field distribution for a nanoslit-coupled HMM Ag-SiO$_2$ multilayer. From bottom to up, layers are [30 nm Cr, 10 nm SiO$_2$, 6 × {15 nm Ag, 15 nm SiO2}, 50 nm Si$_3$N$_4$}. Three operating wavelengths are simulated. Up: 500 nm; Middle: 600 nm; Bottom: 750 nm.

3.2 Multilayer Sample Preparation

A nanoslit-coupled HMM device requires nanostructures to be fabricated on both top and bottom side of the HMM. On one side, a series of nanoslits are made to couple incident light into the HMM, generating the sub-diffraction illumination beams. On the other side of HMM, nanostructures are designed and fabricated as artificial scattering objects, which will scatter the near field illumination pattern to the far field detecting device. By designing special artificial objects, the space-to-spectrum transformation can be measured from far field.

The sample consists of a layer of Cr mask, an HMM made by multiple pairs of Ag and SiO$_2$, and a Si$_3$N$_4$ layer as illustrated in figure 3.2a. The fabrication process starts from a Si$_3$N$_4$ membrane window (figure 3.2b) (4104SN-BA, SPI Supply Inc.). Six pairs of Ag-

SiO$_2$ (thickness per layer: 14 nm, ratio: 1:1) is deposited on the 50-nm thick Si$_3$N$_4$ membrane. Then the HMM is covered by a 40 nm Cr layer. All layers are deposited by magnetron sputtering (AJA International Inc.). The quality of hyperbolic metamaterial is examined by imaging its cross-section by FIB-SEM (FEI Scios DualBeam), to make sure the Ag and SiO$_2$ layers are well separated from each other (figure 3.2c). The same focused ion beam (FIB) is then used to make nanoslits on both sides of the sample. Straight lines (~few microns long) are milled on the Cr mask to couple light into HMM. The SEM image of the milled straight line shows a line width ~27 nm (figure 3.2d). The 50-nm thick Si$_3$N$_4$ layer is used as the artificial object layer. Two different objects are milled into it by FIB, firstly to measure the space-to-spectrum transformation, and secondly to prove imaging resolution.
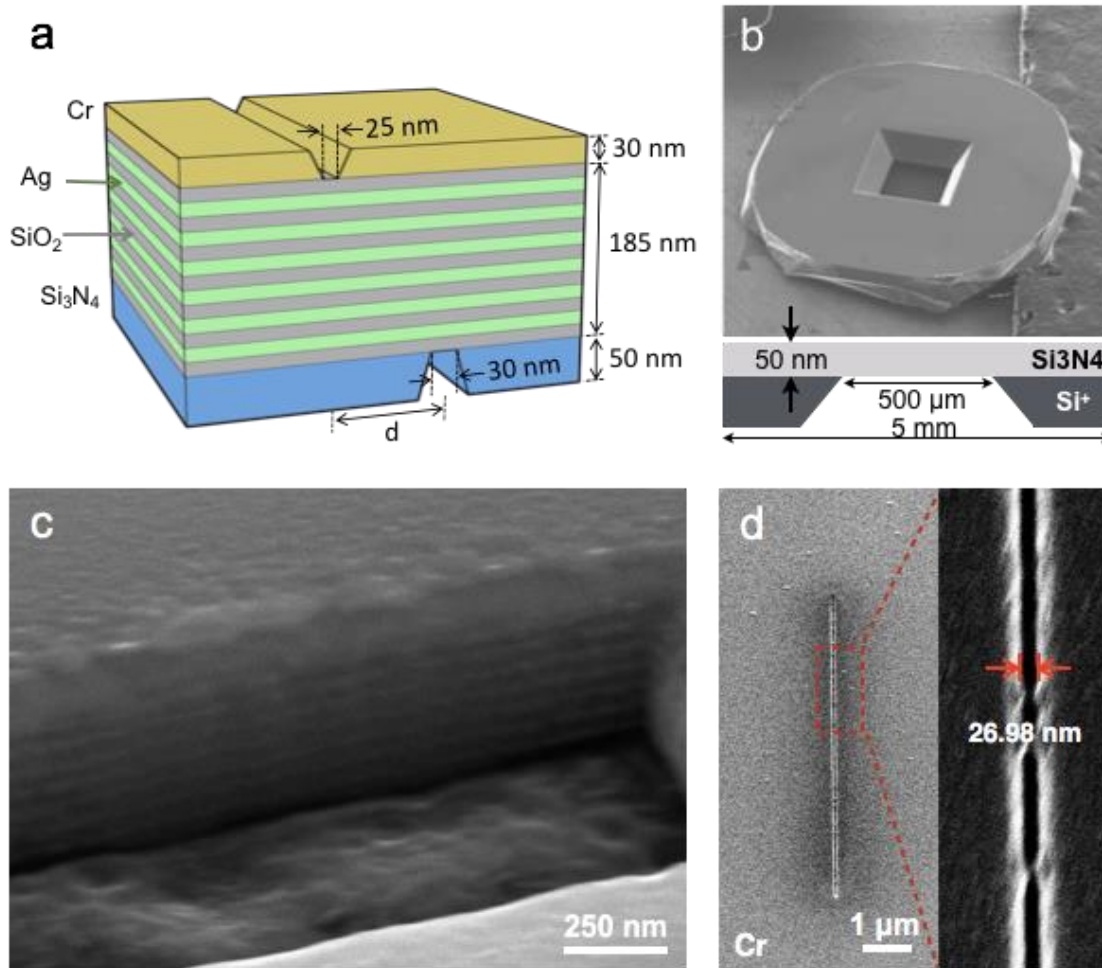
Figure 3.2: Sample of Nanoslit-coupled multilayer HMM. (a) Schematics of multilayer HMM deposited on a Si_3N_4 Membrane window. The multilayer consists of Ag-SiO_2 stacks (6 pairs; thickness of each layer, 14nm). Air slits in Cr mask and Si_3N_4 Membrane are made by FIB. Width of air slit is ~25nm on Cr side and is ~30nm on Si_3N_4 side. Slit in Cr layer is used to couple into HMM, slits in Si_3N_4 are used as artificial object. (b) Sketch and SEM image of a Si_3N_4 Membrane window. The window size is 0.5 mm. The membrane thickness is 50 nm. Reprinted from websites: https://www.2spi.com/. (c) FIB-SEM cross-section image of Ag-SiO_2 stacks. (d) SEM image of 10 um long slit on Cr side.

3.3 Experimental setup of MAIN

Figure 3.3 illustrates our dark-field microscope experimental set up, which measures far field scattering signal from the artificial object. The testing system consists of a nanoslit-coupled HMM sample, a transmission mode dark-field microscope, a broadband light source, and a tunable bandpass filter. The HMM sample, when illuminated by white light, projects sub-diffraction-limited wavelength-dependent patterns onto the object that lies at its top surface. The object, interacting with those near-field patterns, scatters light to the far field which is later collected by diffraction-limited optics,

$$I(\boldsymbol{r}, \lambda) = P(\boldsymbol{r}, \lambda)O(\boldsymbol{r}) \otimes PSF(\boldsymbol{r}, \lambda), \tag{3.1}$$

where I is the hyperspectral image detected at far field, P is near field illumination patterns, O is the object, and PSF is the point spread function of the imaging system. Therefore, the object O can be retrieved by the spectral data I with known illumination patterns P. In this specific case when a single nanoslit is used to in-couple illumination, $P(\boldsymbol{r}, \lambda)$ looks like a nanoscale 'rainbow' with its size and wavelength dependency determined by the dispersion of the HMM. The dark field configuration is used to only detecting signal from scattering objects and to avoid direct transmission light though the unpatented area of HMM sample.
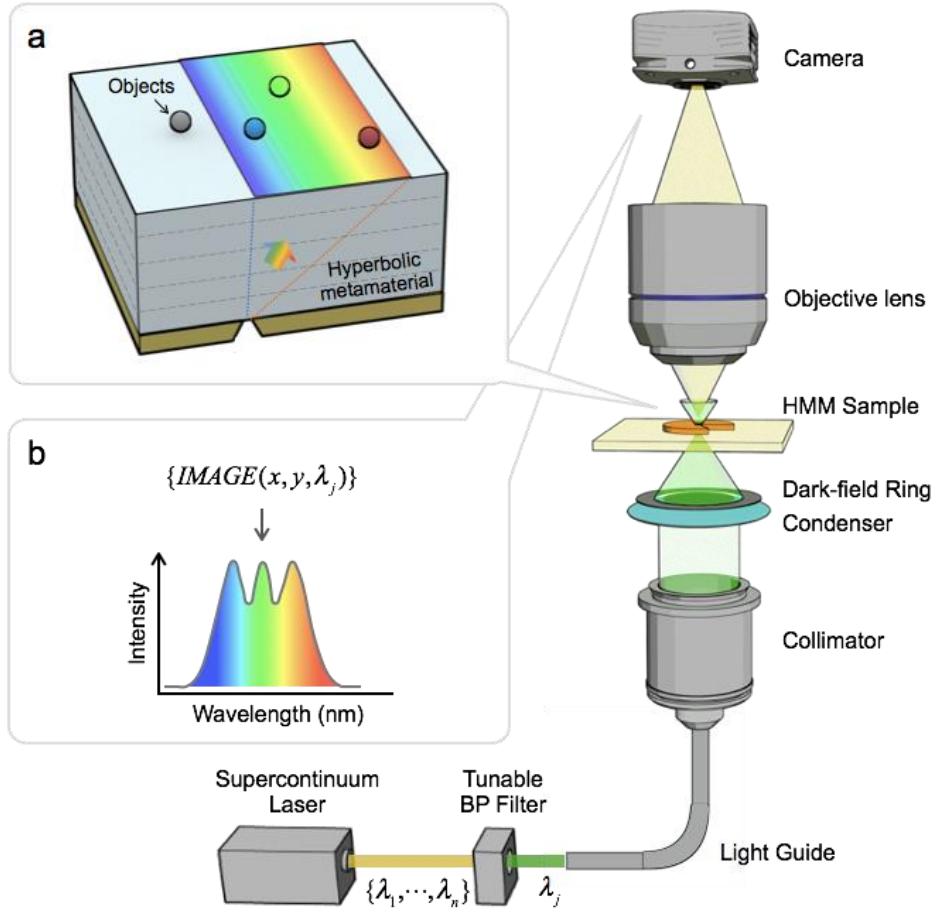
Figure 3.3: Hyper-structured illumination and its experimental setup. (a) The hyperstructured illumination device has incoming light coupled through a nanoslit. The HMM then splits the in-coupled beam into multiple wavelength-dependent directions and projects a nano-scale "rainbow" on its top surface. The objects, illustrated as a few spherical particles, are illuminated by the rainbow. (b) Scattering signal from particles at different positions have a different wavelength, respectively. The hyperbolic metamaterial (HMM) sample is imaged under a conventional microscope in dark filed configuration. A supercontinuum laser, equipped with a tunable bandpass filter, which serves as a light source, scans its output wavelength in serial while the HMM sample is imaged by a camera to form a hyperspectral image $I(r, \lambda)$. Dark field mode ensures that only scattered signal (drawn in light yellow) from the objects (on top of HMM sample) is collected, while direct transmission through HMM (drawn in green) is not collected.

3.4 Verification of Space-Spectrum Transformation

The first artificial object is designed to experimentally measure the space-to-spectrum transformation. A ~10 μm long line is milled into a Si_3N_4 membrane to interact with one of those two symmetrical near field "rainbow" pattern generated by the single nanoslit on the Cr mask. A small tilting angle (α=1.51 degree) between the slits either side of the HMM makes the lateral separation **d** changes along **y** direction, as illustrated in figure 3.1a and imaged by scanning electron microscope (SEM) in figure 3.4c. The sample is measured by a dark field microscope shown in figure 3.2 (illumination source: SuperK Extreme EXB-6, objective lens: 50X/0.5, camera: Andor iXon 897).

Based on the HMM dispersion property, as **d** increases, the spectrum of this tilted line shifts to longer wavelength. This phenomenon is firstly observed from a RGB image (figure 3.4b) in the far field and then quantitatively analyzed by measuring the spectral shifts of the titled line along **y** directions (figure 3.4d). The spectrum is measured by firstly taking a diffraction-limited spectral image,

$$I(x, y, \lambda) = O(x, y)P(x, \lambda) \otimes PSF(x, y), \tag{3.2}$$

then integrating along x direction,

$$S(\lambda, y) = \int I(x, y, \lambda)dx. \tag{3.3}$$

The hyperspectral image is taken by stepping the tunable bandpass filter from 460 nm to 840 nm with a step of 10 nm. Selected spectrums at indicated locations are plotted in figure 3.4d. For each spectrum in $S(\lambda, y)$, we find the peak wavelength and plot it as function of separation **d** based on the known geometrical relationship between **y** and **d**,

$$\Delta d = \Delta y \cdot tan(\alpha). \qquad (3.4)$$

A red shift of spectral peaks can be observed when y (and d) increases, which stands for spatial-spectral mapping of this specific device. The curve (red dot) matches with the dispersion curves (blue) predicted from simulation, while a small detour of red dot from simulation curve indicates distortion of near field illumination patterns.
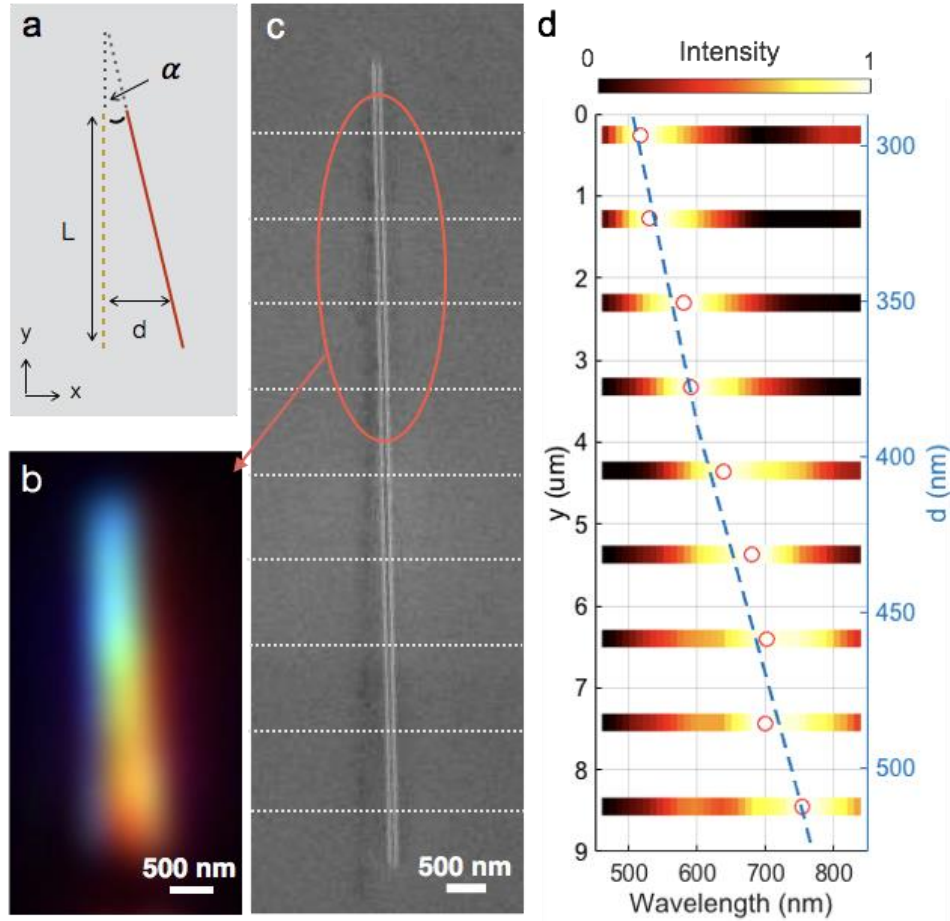
Figure 3.4: Calibration of Spatial-Spectral Transformation. (a) Drawing of the geometrical location of a tilted slit on Si_3N_4 membrane. Dashed line (yellow) represents the location of the coupling slit in the Cr film and the solid line (red) represents object slit in the Si_3N_4 film. The angle a is 1.51 degree (exaggerated in the drawing). L: 10 μm. (b) RGB diffraction-limited image of part of the titled slit. The three channels (RGB) are acquired in serial by setting tunable bandpass filter to [460 nm : 500 nm], [510nm : 570nm], [580nm : 700nm] respectively. (c) Scanning Electron Microscope (SEM) image of entire air slit on SiN membrane. (d) Spectral response along y direction (and distance d along x direction) in (c) at indicated location (white dashed line). Distance d is calculated based on the known geometrical relationship with y. Red dots: peak position of each measured spectrum. Blue dashed line: full wave simulation of near field beam locations versus wavelength for the same Ag/SiO_2 multilayer.

3.5 Super-resolution image

We then use the verified spatial-spectral transformation for imaging reconstruction. The notation of measured hyperspectral image can be rewritten as

$$I(x,y,\lambda) = \iint E(x'-D\lambda - x_0)O(x',y')PSF(x-x',y-y')dx'dy',$$ (3.5)

where $E(x)$ is intensity distribution of the well-confined line-illumination at a single wavelength on the top surface of HMM. The illuminated line has wavelength-dependent locations $D\lambda + x_0$, where D and x_0 are fitted parameters from figure 3.4d. The reconstruction includes two steps: firstly, a series of digital aperture is added on every frame of the hyperspectral image; secondly, all the processed frames are summed to form a super-resolution image:

$$Im(x,y) = \int I(x,y,\lambda)A(x-D\lambda - x_0)d\lambda \approx I(x,y,\tfrac{x-x_0}{D})$$ (3.6)

where A is the digital aperture $(A(x) \approx \delta(x))$ added to every wavelength-frame of the spectral image. Substitute Eq. (3.5) into Eq. (3.6), we obtain

$$Im(x,y) = \iint E(x'-x)O(x',y')PSF(x-x',y-y')dx'dy'$$ (3.7)

Eq. (3.7) can be rewritten as

$$Im(x,y) = O(x,y)\ddot{A}PSF_{eff}(x,y)$$ (3.8)

where PSF_{eff} is the effective point spread function,

$$PSF_{eff}(x,y) = E(x)\times PSF(x,y)$$ (3.9)

The synchronized scan of digital aperture and laser focal spot make the process similar to a confocal laser scan microscope [25,68], but with a much more confined beam width. Since $E(x)$ typically has much smaller FWHM than the point spread function of a

microscope, it has great resolution improvement along x direction. We use a Zeiss 50X/NA 0.5 objective lens in the experiment. Therefore, the FWHM of PSF is around a wavelength. From full wave simulation in figure 3.1, the FWHM of $E(x)$ is ~80 nm when operating wavelength is 500 nm, which mainly determines the resolving power.

To test the imaging resolution, we image a tilted line-pair on the Si_3N_4 membrane shown in figure 4.4. The objects are made by FIB milling. The spectral image is taken by the same experimental set-up in figure 3.3. The dispersion coefficient D is ~0.81 nm/nm (position/wavelength). In the experiment, it is hard to precisely know x_0, which is related to the location of the slit on the Cr mask. Fortunately, a small misalignment of x_0 won't affects the resolving power [25]. For the imaging reconstruction in figure 3.4, a scan of x_0 is performed and the final x_0 is manually selected based on the quality of the reconstructed images.

As observed from the SEM image, the two slits gradually merge. A similar optical image is reconstructed. The intensity cross section reveals that our MAIN method can resolve down to ~84 nm, which is already close to the simulated FWHM of the tested multilayer system. When the two slits are too close, it becomes a single deep slit milled into the HMM layer. The deep slit dramatically changes the dispersion relationship, causing a defect at the bottom part of the reconstructed optical image.

The imaging reconstruction forms a super-resolution image without knowing the exact shape of $E(x)$, which might be affected by HMM and nanoslit quality and is hard to measure directly from the far field. Only the dispersion property of the HMM needs to be calibrated. It is worthy to note that wavelength-dependence of point spread function

PSF(x,y) and pattern E(x) is ignored in above notations. In practice, the wavelength dependence will result in a spatially variant effective point spread function.
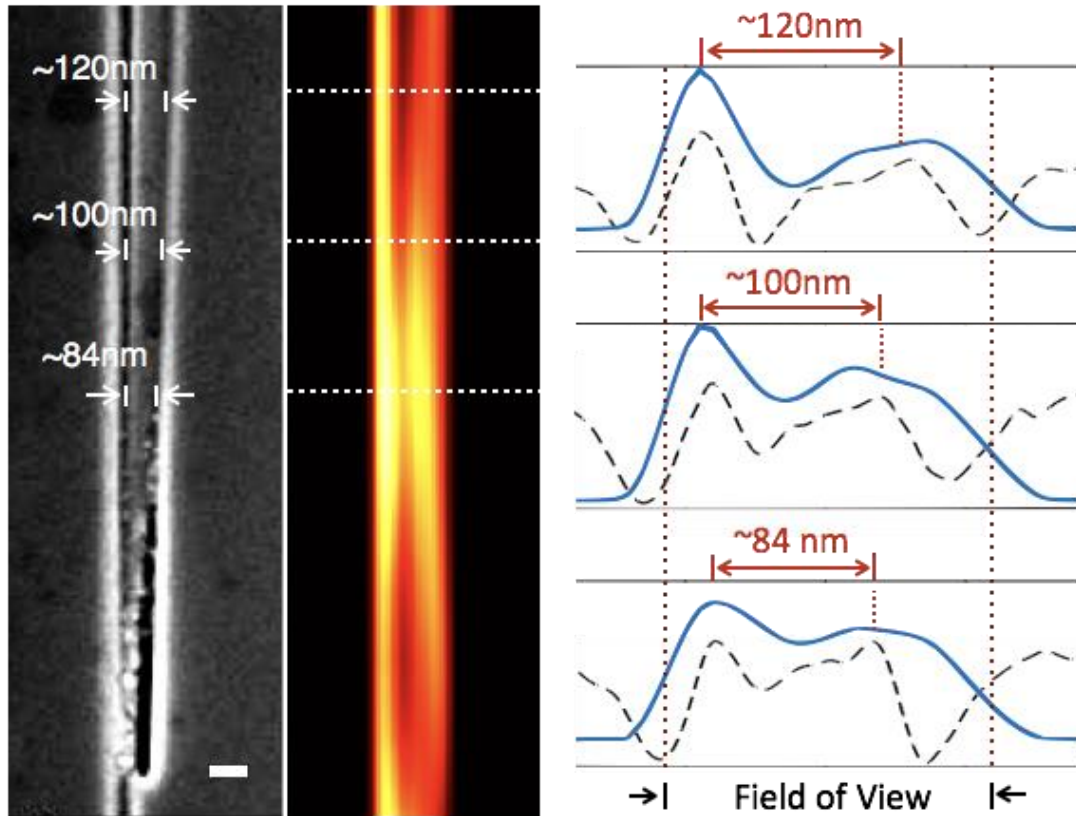
Figure 3.5: Super-resolution image demonstration. Left: SEM Image of a tilted pair of slits milled into Si₃N₄ layer. Slit width: ~35nm. Middle: Super-Resolution image. Right: Cross-section of the image at indicated locations. Blue solid line: super-resolution image; black dashed line: SEM image (inverted). Scale Bar: 100nm. The Field of View is affected by the wavelength range of the hyperspectral image. Wavelength Range: 460 nm:700 nm

3.6 Conclusion

We studied an Ag/SiO_2 hyperbolic metamaterial to be used as metamaterial-assisted illumination microscope (MAIN) with 1D resolution improvement. By making artificial structures on both sides of the HMM, we characterize its material dispersion and show a 1D super-resolution image from a hyperspectral image acquired at far field. This study shows that hyper-structured illumination is practically feasible, which provides an alternative method for non-fluorescent super-resolution surface imaging.

The resolution is mainly determined by the highest spatial-frequency wave a HMM can carry, and it is proportional to the unit pair size of a HMM multilayer [39,57]. For Ag/SiO_2 system, a unit pair size of 20 nm is practically achievable by sputtering method, which can bring the resolution down to ~50 nm. Other than that, epitaxial growth metamaterial system can have its unit pair size down to few nanometers [69], which can dramatically improve the resolution.

Another practical concern of imaging is about the accuracies to estimate near field illumination patterns. Distortion of near field patterns happens when there is imperfection in multilayer and nanofabrication (as we observe in figure 3d). Fortunately, sophisticated reconstruction method [26] can reconstruct a super-resolution image without fully known illumination patterns. Works along this direction greatly reduce the strict requirement on knowing the exact near field patterns and make use near field patterns for structured illumination practically feasible.

Chapter 3, in part, has been submitted for publication of the material as it may appear in Nature Communications, 2018. Q. Ma, H. Qian, S. Montoya, W. Bao, L. Ferrari, H. Hu, E. Khan, Y. Wang, E. Fullerton, E. Narimanov, X. Zhang, Z. Liu, "Experimental

demonstration of hyperbolic metamaterial assisted illumination nanoscopy". The dissertation author was the first author of this paper.

Chapter 4

Widefield metamaterial-assisted speckle illumination microscope

This chapter presents a two-dimensional wide-field super-resolution imaging method based on hyperbolic metamaterial assisted illumination, named metamaterial-assisted speckle illumination nanoscope (speckle-MAIN). Unlike the nanoslit/nanohole-coupled HMM in the previous chapters, a new coupling method is investigated to conveniently provide illumination pattern with deep subwavelength resolution on two-dimensions when a light passes through a HMM. The new coupling method relies on the intrinsic scattering inside a Ag-SiO$_2$ multilayer HMM that is caused by non-flat interfaces between sputtered silver and silica layers. Simulation shows that the speckle-like illumination patterns that has resolution 5 times higher than the diffraction-limit will be generated after light passing through the multilayer HMM. Experiment demonstrates that the speckle-MAIN can resolve two dots down to ~60 nm, by using a relative low NA objective lens, and hence, a wide field of view. Characteristic features of the speckle-MAIN were simulated, and the results are in good agreement with the measurements.

4. 1 Motivation of speckle-MAIN

Structured illumination microscope is one of the most prevailing techniques to go beyond the diffraction limit. Compared with other approaches including molecule localization [8] or STED/RESOFT microscope [6,70], SIM has been proven to have supreme advantages in high spatial-temporal resolution associated with low photo-toxicity [14,21,71].

The resolution of SIM, however, is limited by its highest spatial frequency of illumination and detection:

$$f = f_d + f_i \, , \tag{4.1}$$

where f is the cut-off spatial frequency of SIM, f_d and f_i are the maximum spatial frequency of detection optics and illumination patterns, respectively. By using far-field optics, SIM only extends the resolution by a factor of ~2 because both illumination and detection bandwidth are diffraction-limited.

To further extend the resolution, researchers work on extending the spatial-frequency f_i of illumination patterns. For instance, Nonlinear SIM [13], by saturated exciting fluorophores, can greatly increase f_i. However, it requires strong laser intensity to excite the fluorophore, which commonly are associated with high phototoxcity and photobleaching.

The resolution of illumination patterns can also be increased by material if only specimen on the substrate surface to be imaged. For instance, TIRF-based SIM [72] can take advantage of the refractive index of the substrate, generating an illumination pattern with slightly smaller period than what is in air. The improved resolution can be further

extended to if especial substrate material such as GaP is used [73], while the resolution is still limited by the material itself.

Ag-SiO$_2$ multilayer, well known as an artificial hyperbolic metamaterial (HMM), is capable to project illumination patterns that has almost unlimited resolutions in theory. Figure 4.1 presents that hyperbolic metamaterial, benefiting from its anisotropic hyperbolic isofrequency curve, is capable of carrying much higher spatial frequency content than conventional materials. We show the comparison among isofrequency curve of air, an 'ideal' HMM and a practical HMM multilayer in figure 4.1a. The ideal HMM has unlimited bandwidth of spatial frequency (k_x), while a practical HMM made by Ag-SiO$_2$ multilayer, will have bandwidth limitation due to its periodicity [39]: multilayer with smaller unit thickness will support higher spatial frequency. A practically achievable Ag/dielectric multilayer with a period of 20 nm [74], supports highest-k mode at ~10k$_0$.

Despite that the supported bandwidth of spatial frequency is high, a coupling method is required to match the momentum difference between free space incident light (typically low-k) to the high-k wave mode inside HMM. In this research, we study the possibility to use intrinsic scattering caused by non-flat interface between sputtered silver and silica layers, drawn in figure 4.1d, to generate speckle generation at its HMM top surface. It turns out that the speckles from intrinsic scattering can be ultrahigh resolution and can be controlled at far field by incident angle and wavelength as shown in figure 4.1c. In the following sections, we firstly characterize the optical property and morphology of the Ag-SiO$_2$ multilayer made by sputtering deposition method. Secondly, we simulate the effect of non-flat interface in generating the near field illumination patterns. Lastly, we

demonstrate resolution improvement by illuminating fluorescent beads and quantum dots
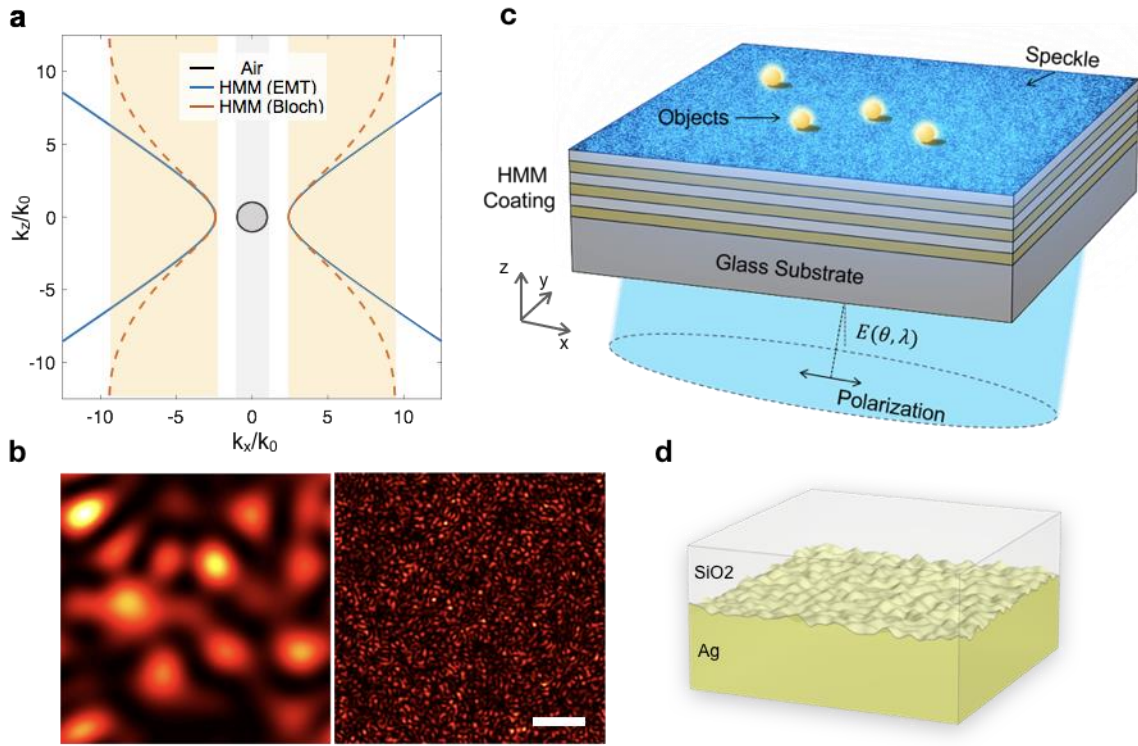
by those patterns.

Figure 4.1: Metamaterial-assisted speckle illumination. (a) Isofreqeuncy curve of air, ideal hyperbolic metamaterial by effective medium theory (EMT), and practical hyperbolic metamaterial consists of periodical layered structures of Ag and SiO_2 (Bloch). The wave vector k_x and k_z are both normalized to the wave vector in air k_0. The allowed k-bandwidth is highlighted in gray (air) and in orange (practical hyperbolic metamaterial). Permittivity of ideal hyperbolic metamaterial is (ϵ_x = -2.5718, ϵ_z = 6.0256). Permittivity of practical HMM (ϵ_{metal}= -7.2840 , $\epsilon_{dielectric}$ = 2.1405, t_{metal} = 10 nm, $t_{dielectric}$ = 10 nm). (b) Simulated speckle patterns from diffraction limited optics (gray bandwidth in c) and a practical hyperbolic metamaterial (yellow bandwidth in c). Scale bar: 400 nm. (c) A metamaterial coated substrate projects ultra-fine structured patterns onto objects lying on its top surface. (d) Schematics of the non-uniform interface between sputtered Ag and SiO_2 interface.

61

4.2 Multilayer HMM Deposition and

Characterization

Ag-SiO$_2$ multilayer, composed of 3 pairs of 10 nm Ag and 4 nm SiO$_2$ layers, were prepared by alternately DC magnetron sputtering and RF magnetron sputtering at room temperature. Sputtering rates for Ag and SiO$_2$ at 200W were ~1 nm/s and ~0.8 nm/min, respectively. The rate is determined by TEM image of the sample crosssection. The pressure of the chamber was 2.5 x 10^{-6} mtorr and the Ar pressure was at 3.2 mtorr for silver and 5 mtorr for SiO2 during the deposition, respectively. The glass substrate (VMW Micro cover glasses, No.1 1/2) is cleaned by Acetone, IPA, and water for several times and dried by compressed air. An adhesion layer (<1 nm thickness) of Cr is deposited prior to the deposition of Ag-SiO$_2$ multilayer. The sputtering machine is Denton discovery 635 at nano3 facility of Calit2, UCSD.

Figure 2 presents the characterization of this multilayer HMM. Its optical transmission/reflection at normal incidence is measured and then compared to theoretical calculation using bulk material property (figure 4.2a). We measured that, when the silver thin-film is below 10 nm, the transmission of HMM will be different from the calculated ones. This indicates a low-quality silver film and a different material property i.e. permittivity from the bulk ones. We select 10 nm film for silver to ensure the accuracy of our simulation by using bulk silver material properties in the following sections. Atomic force microscopy (AFM) is used to measure the top morphology of the deposited multilayer (figure 4.2b). The roughness (RMS) of the multilayer is measured to be ~ 1.1 nm, and the correlation length of the rough surface is 35 nm. A transmission electron microscopy (TEM)

image presents the well-formed periodic structure in the Ag-SiO$_2$ multilayer. The non-perfect interface of these two amorphous thin films can also be observed.
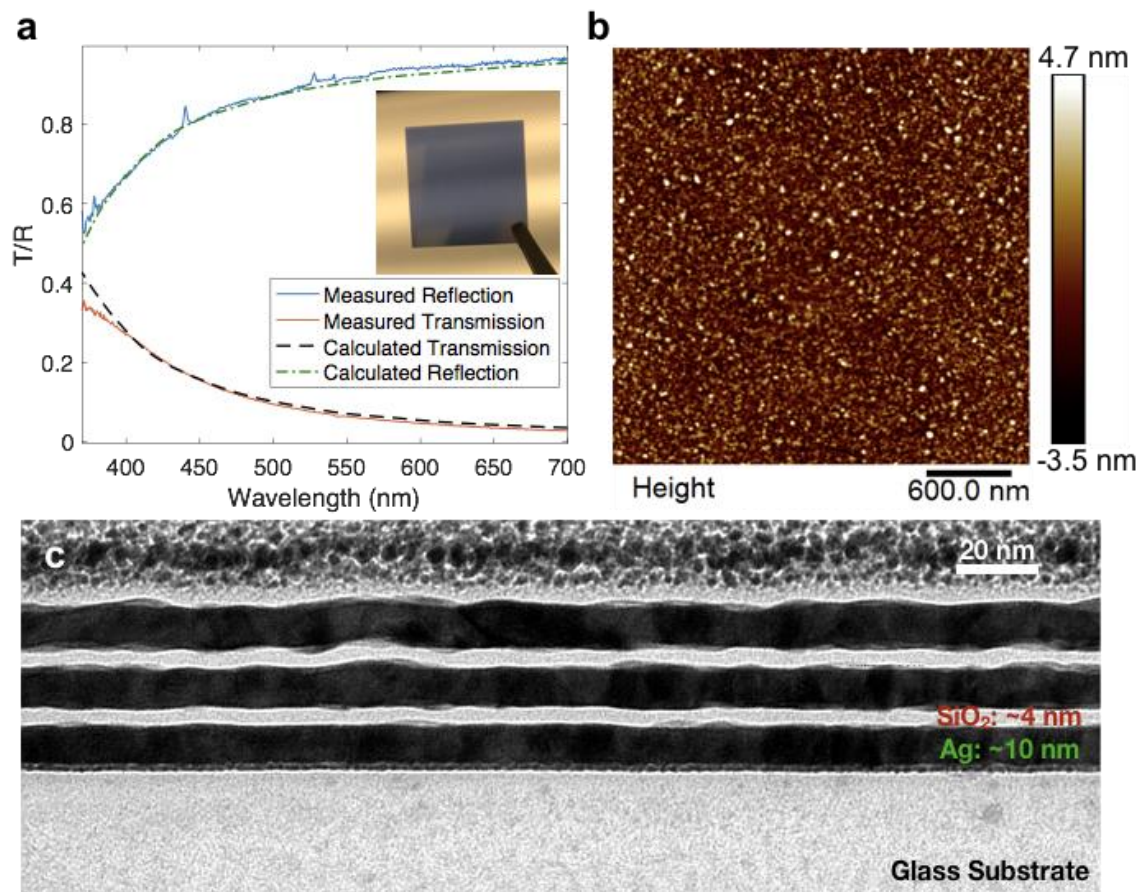
Figure 4.2: Material characterization. (a) Transmittance and reflectance at normal incidence of Ag-SiO$_2$ multilayer. Inset image: a photo of the Ag-SiO$_2$ multilayer-coated coverglass. Calculation is done based on transfer matrix method for 3 pairs of {11 nm Ag and 4 nm SiO2}. (b) AFM image of top surface. Scan area: 3 um x 3um (512 x 512). (c) TEM Cross-section shows 3 pairs of Ag and 4 nm SiO2 on top of a glass substrate with Cr adhesion layer.
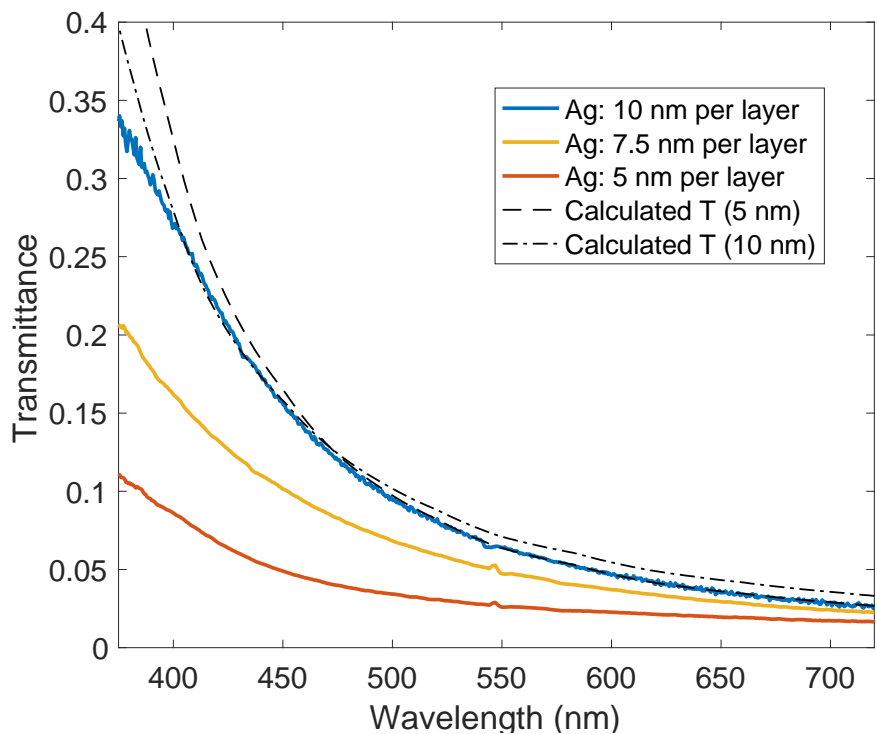
Figure 4.3: Transmittance of Ag-SiO$_2$ multilayer with different silver layer thickness. Blue solid: measured transmittance of 3 pairs of 10 nm Ag and 4 nm SiO$_2$. Yellow solid: measured transmittance of 4 pairs of 7.5 nm Ag and 3 nm SiO$_2$. Red solid: measured 6 pairs of 5 nm Ag and 2 nm SiO$_2$. Black dashed: calculated transmission of 3 pairs of 10 nm Ag and 4 nm SiO$_2$. Black dot-dashed: calculated transmission of 6 pairs of 5 nm Ag and 2 nm SiO$_2$.

4.3 Simulation of multilayer with rough interface

4.3.1 Generation of rough interface

To foresee the effect of small roughness at the interface on generating speckles, a full wave simulation modeling with measured film roughness is used. The results of the simulations presented here are based upon solution of coupled Maxwell's equations. Finite difference time domain (FDTD) method was employed using Lumerical software. In experiment, the structure is excited by electromagnetic wave with different polar and azimuthal angles in spherical coordinates from the bottom of the structure in z-direction (See Fig. 4.1c). In the simulation, it would suffice to excite the HMM using x-polarized plane electromagnetic wave with wavelength λ and varying polar angle θ in order to observe the localized features. We incorporated local bulk dielectric functions of Ag from Ref [75]. The refractive index of SiO_2 was chosen to be equal to 1.46. The matrix was chosen as air like in experiment. The next step is to consider the non-flat or random rough surface. For our purpose, it is important to model the rough surfaces accurately to describe the main characteristics observed in experiment. Topographic features of a random rough surface are characterized mainly by a root mean square (RMS) as a measure of the magnitude of varying height and correlation length (Cl) in two dimensions where the surface is defined [76]. Based upon our AFM measurement, we chose RMS = 1.1nm and Cl = 35nm to model the random rough surfaces (See figure 4.4 for the code-generated

rough surface). After the structure is excited by the incident light, the enhanced localized

intensity is calculated about 10nm above the top surface of the structure.
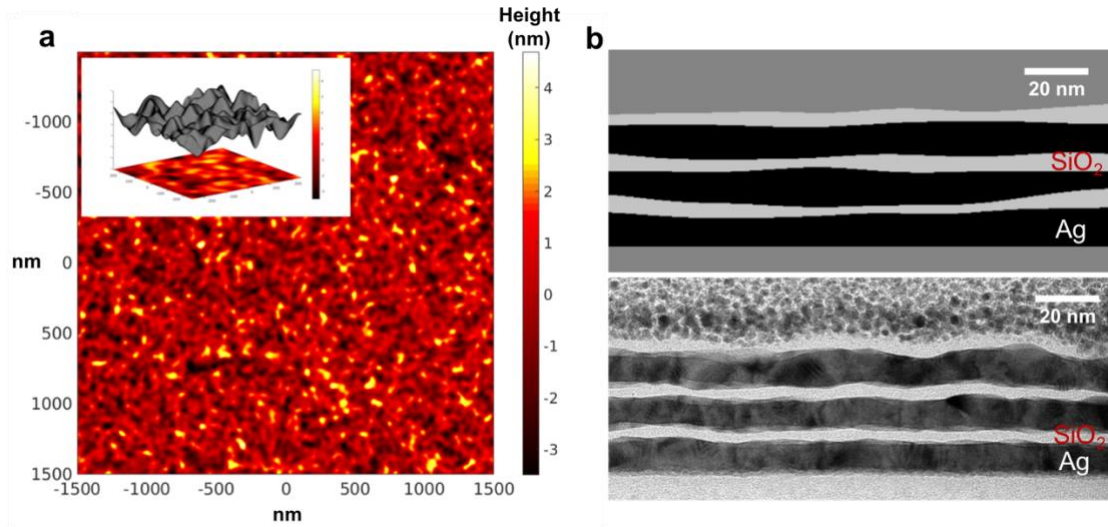

Figure 4.4: Code-generated rough surface. (a) 3D morphology of roughness and top view of the rough surface with RMS=1.1 nm and correlation length of ~35 nm. (b) Side view of the structure showing three pairs of Ag and SiO_2 with thicknesses of ~ 10 nm and 4 nm respectively. Black: Ag; Gray: SiO_2.

4.3.2 Near field illumination patterns

We excite the HMM using x-polarized plane electromagnetic wave with wavelength λ and varying polar angle θ. The speckles, represented by the absolute value of electric field distribution 10 nm away from the top surface of HMM are simulated with a series of wavelengths and incident angles. Figure 4.5 presents a three selected $|E|^2$ distribution at (500 nm, 0 degree); (500 nm, 45 degree) and (600 nm, 0 degree), respective, demonstrating that the speckle has ultrahigh resolution and can be controlled by tuning either wavelength or angle/phase.

We mainly care about two parameters of the speckles $|E|^2$: its maximum spatial frequency content and the independence between different speckles. The first one is analyzed based on the magnitude transfer function (MTF) of the $|E|^2$ (Figure 4.6). The latter can be analyzed by the cross-correlation between the speckles (Figure 4.7). According to figure 4.6, a HMM-assisted speckle illumination has much wider spatial frequency bandwidth compared to the speckles generated in air. While the speckles in the air has steep cutoff frequency at *$2k_0$*, the spatial frequency of HMM-assisted speckles decays gradually when k_x is larger. Presuming that a signal noise ratio (SNR) from 100 to 1000 is achievable in a practical imaging system, speckles generated by HMM (3 pairs, 20 nm unit size) can extend the spatial frequency to $6k_0$ (SNR = 100), *$10k_0$* (SNR =1000), respectively. As mentioned in Ref [57], the unit cell size of a multilayer HMM will also affect the resolution of speckles. Generally, a multilayer HMM with thinner unit pair size will have speckles with higher-resolution, as can be seen by the MTF comparison between a 10 nm unit size multilayer and a 20 nm unit size multilayer. However, the unit pair size is limited by the minimum achievable silver film thickness in thin film deposition process.

The correlation between speckles drops to 0.5 with ~15-degree incident angles difference. Consider the illuminating system is a linear system with complex electric field, intensity distribution can be generated from the phase difference between different incident angles. To conveniently generate enough distinguishable speckles, we illuminate the HMM with a random, diffraction-limited optical field generated by either a diffuser or a multimode fiber. The complex field (diffraction-limited speckles), equaling to a composite of plane waves at different angle and phase, will convert into sub-diffraction limited speckle after passing through the HMM.
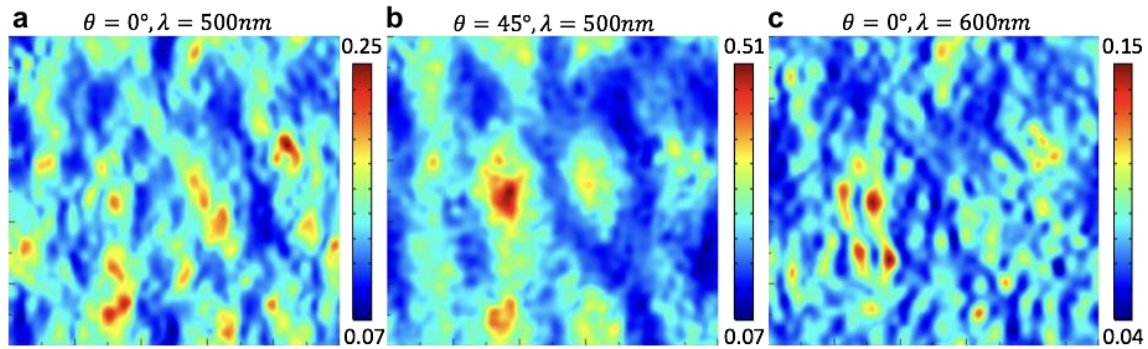
Figure 4.5: Simulated intensities on x-y plane at 10nm on top of the structure for surface area windows of $1\mu m \times 1\mu m$ for (a) $\theta=0°$, $\lambda=500nm$, (b) $\theta=45°$, $\lambda=500nm$, and (c) $\theta=0°$, $\lambda=600nm$.

Figure 4.6: MTF of generated speckles. The speckles are calculated 10 nm away from HMM top surface. Blue: 3 pairs of HMM with 20 nm unit pair size (fill ratio: 1:1); Red: 6 pairs of HMM with 10 nm unit pair size (fill ratio: 1:1). Wavelength: 500 nm. Black: MTF of laser speckles in the air.

Figure 4.7: Normalized cross-correlation between speckles at different incident angles. (3 pairs, 20 nm unit size, 1:1 ratio).

4.4 Speckle-MAIN setup

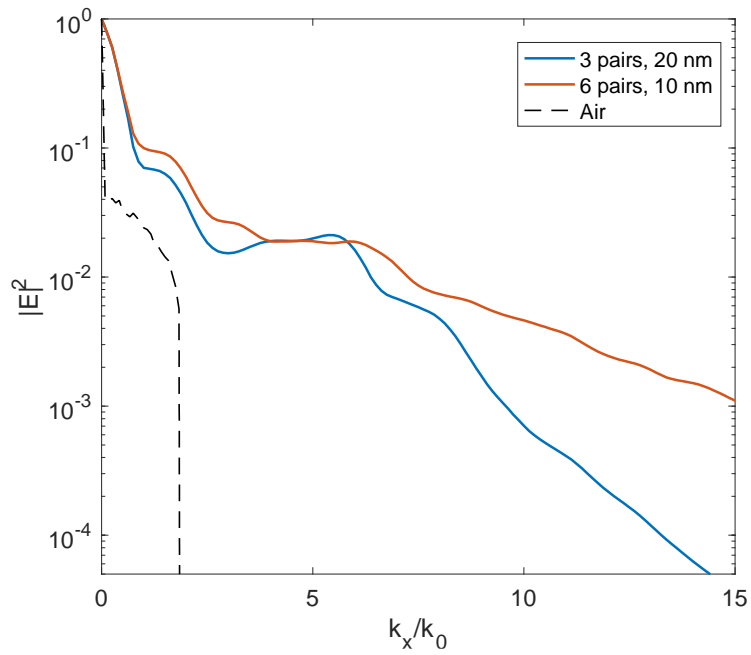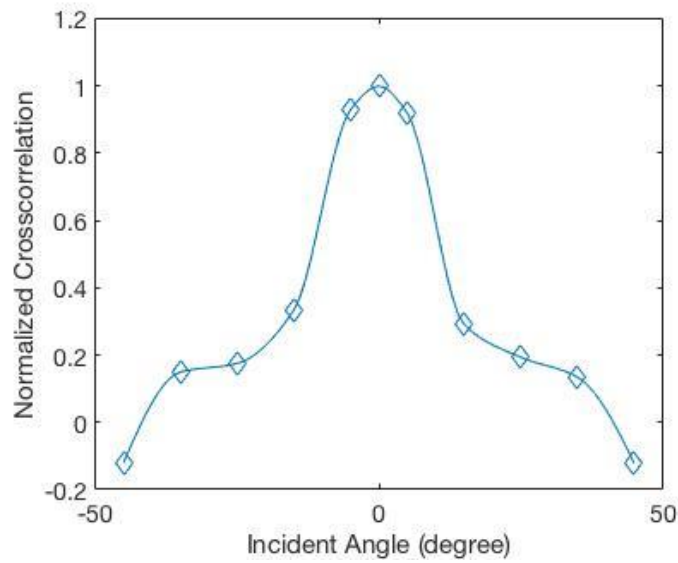To demonstrate the high-resolution of speckle patterns experimentally, we image sparsely-distributed fluorescent beads (Fluoresbrite YG Carboxylate, 46 µm diameter) drop-casted on the HMM-coated substrate. A laser, directed by a multi-mode fiber, illuminates on the other side of the substrate. The incident optical field is scrambled due to the multi-mode inference and can be changed by adding vibration on the fiber. The incident field has numerical aperture (NA) of ~0.2. Based on the simulation, the illuminating field on the fluorescent beads will have much higher resolution after passing through the HMM.

Figure 4.8 presents the schematic and photos of experimental set up: a 488 nm laser (Coherent Genesis) are coupled into a multimode fiber (Thorlabs, core diameter: 50um, NA 0.2). The other end of the fiber is coupled to a reflective fiber collimator that is attached to a custom-made adapter of the microscope condenser. The fiber end is imaged to the multilayer HMM, projecting diffraction-limited speckle patterns. The speckle is controlled by a stepper motor which will stretch the fiber spool during image acquisition to have speckles changed. A sCMOS camera is used for imaging acquisition (Hamamatsu Flash 4.0)
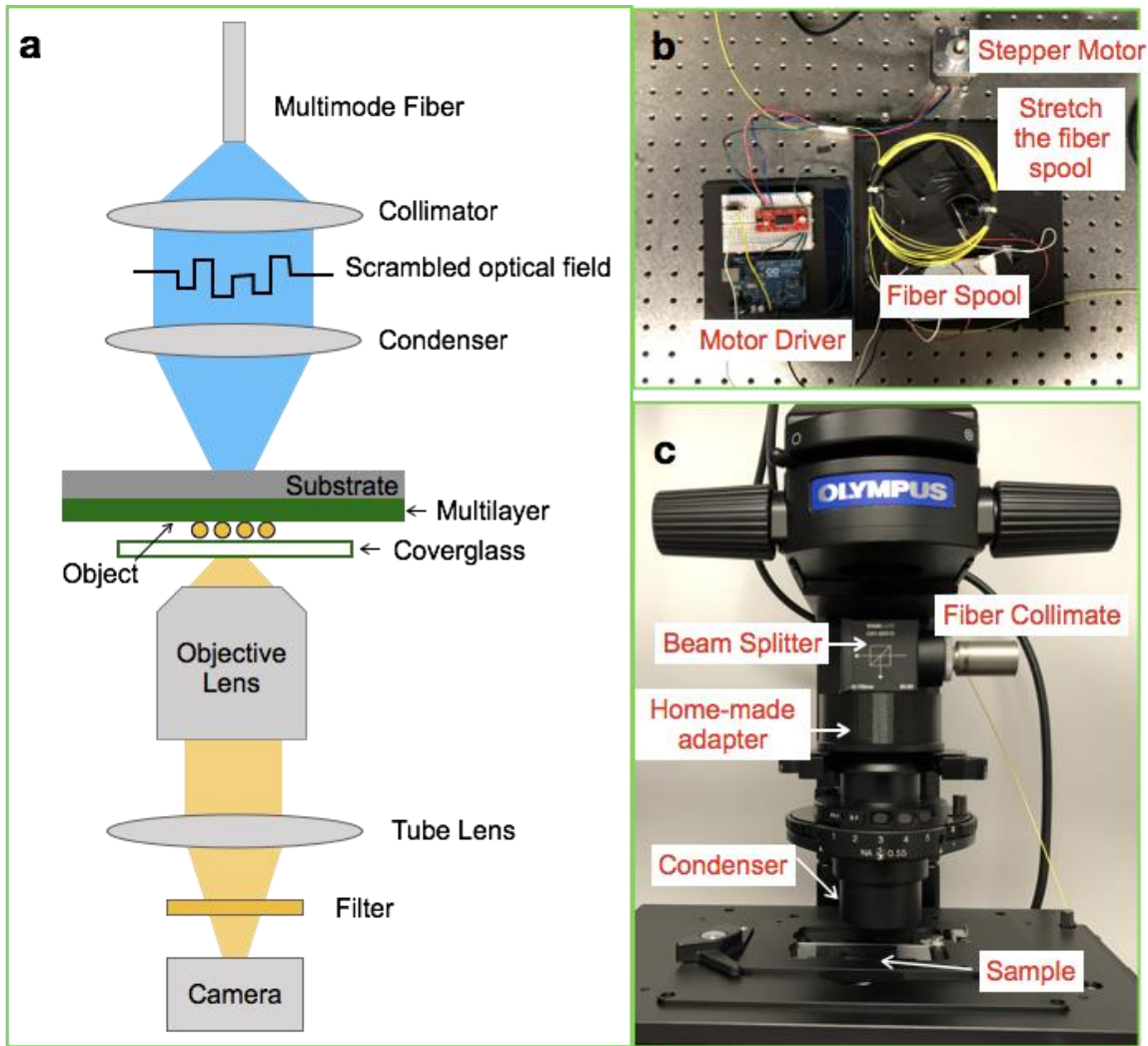
Figure 4.8: Speckle-MAIN Experimental setup. (a) Sketch of essential optical components. (b) Speckle Generator based on multimode fiber. A laser beam is guided by the multimode fiber to an inverted microscope. The multimode fiber spool (tens of loops) is stretched by a stepper motor to change the output optical field. (c) Home-made adapters to an inverted microscope condenser. The adapter, together with the multi-mode fiber system, and multilayer-coated sample substrate, converts the epi-fluorescent microscope into speckle-MAIN.

4.5 Imaging reconstruction

While the simulation tells that the illumination patterns of speckle-MAIN can have much higher resolution than the diffraction-limit, the speckle patterns cannot be precisely estimated or measured in experiment. Fortunately, researchers have shown that the super-resolution capability of structured illumination microscope is not affected even if the patterns are unknown. Iterative codes, by applying certain constraints on the object and the illumination patterns, are capable to retrieve a super-resolution image of object from a series of unknown illumination.

There are two algorithms used in this chapter: Blind-SIM [26] and Block-FISTA [77]. The two algorithms differ from the applied constraints of object/illumination. For blind-SIM, the constraint is on the illumination pattern that all illumination patterns add up to a uniform pattern; for block-FISTA, the constraint is on the object that the object is sparse. The cost functions of Blind-SIM and Block-FISTA are explained in the following two sections, respectively.

In experiment, each super-resolution frame is reconstructed from multiple sub-frames ($80-500$ frames) with different incident electrical field. The reconstruction costs $10-30$ mins on a NVidia GTX 1080 Ti graphic card.

4.5.1 Blind-SIM Algorithm

Blind structured illumination microscopy (Blind-SIM), reconstructs a super-resolution image with same resolution capability of conventional SIM while Blind-SIM uses unknown diffraction-limited speckle illumination [26]. The Blind-SIM code is an l_2-

norm based minimization algorithm that jointly recovers the object and illumination through minimizing the cost function:

$$F\left(obj, I_{i=1,2,\ldots,M}\right) = \sum_{i}^{M} \left|\left|im_i - (obj \cdot I_i)\otimes PSF\right|\right|^2,$$ (4.2)

where im_i and I_i is the ith image and i^{th} illumination pattern, respectively, PSF is the point spread function of the imaging system, obj is the object and M is total number of measurements. Two constraints are used to minimize the cost function: (1) The object is positive; and (2) The summation of M illumination patterns equals to uniform illumination. Applying the second constraint makes the Eq. [4.2] become

$$F\left(obj, I_{i=1,2,\ldots,M}\right)$$

$$= \sum_{i}^{M-1} \left|\left|im_i - (obj \cdot I_i)\otimes PSF\right|\right|^2$$ (4.3)

$$+ \left|\left|im_i - \left(obj \cdot (\sum_{i}^{M} MI_0 - I_i)\right)\otimes PSF\right|\right|^2,$$

where I_0 is a uniform illumination pattern. In experiment, a large number of speckles, and hence, a large number of measurements, are required to statistically make the uniformity constraint to be true. In ref [26], about 150 frames are used to reconstruct a super resolution image when the object is illuminated by laser speckles.

4.5.2 Block-FISTA Algorithm

Block-FISTA is another iterative algorithm to retrieve object from a series of unknown illumination patterns. It was developed for photo-acoustic imaging in which the illumination pattern (from light) is far beyond the detection spatial frequency bandwidth

(from acoustics). The algorithm minimizes the error defined in Eq. 4.2 while a sparsity

constraint is applied to the object. It has been demonstrated that, super-resolution recovery

from a signal is possible by prior-knowing that the signal is sparse -- a superposition of a

few (but unknown) elements from a large collection of base signals. Moreover, most

natural images are known to be sparse in some bases. This method does not requires the

uniformity of added up illumination patterns.

The sparsity constraint is applied in Block-FISTA by a joint-sparsity (also known as block-

sparsity) term,

$$||p||_{2,1} = \sum_{i=1}^{N} \sqrt{\sum_{m=1}^{M} |p_m(x_i)|^2}, \tag{4.4}$$

where p_m is the mth illumination pattern times object. M is total number of frames used in

the reconstruction. N is the number of pixels per image.

The cost function is defined as,

$$F(p) = \frac{1}{2}\sum_{m=1}^{M}\sum_{n=1}^{N}|h * p_m(x_i) - y_m(x_i)|^2 + \alpha_1 ||p||_{2,1} + \frac{\alpha_2}{2} ||p||_2^2, \tag{4.5}$$

where y_m is the mth far field measurement (image), h is point spread function. α_1 and α_2

are regulation parameter of the joint sparsity term and a l2 norm term, respectively. The

block sparsity term $||p||_{2,1}$ enforces sparsity and the l2-norm term $||p||_2^2$ improves the

stability. To minimize this cost function defined in Eq. (4.5), an algorithm known as FISTA

is used [78], which runs faster than the conjugate gradient method in Blind-SIM. The

complete algorithm is provided in Ref [77].

4.6 Image results

4.6.1 Proof of sub-diffraction-limited illumination

Figure 4.9 presents a few selected camera frames while incident optical field is changed randomly by the vibrating multimode fiber. The video is taken under a 100X/1.5 oil objective lens to maximize the detection NA. Knowing that the sample is made of fluorescent spheres, the unsymmetrical look of diffraction-limited image indicates the presence of multiple beads. Four selected raw camera frames present an obvious peak location shifts during the acquisition, indicating the changes of illumination patterns at high-resolution. The super-resolution image is reconstructed by using blind-SIM algorithm to compute all the 500 frames. The super-resolution image resolves four beads, with closest two-beads spacing to be 80 nm. The location of the reconstructed four beads are marked on the raw frames, which agrees well with the peak intensity locations of those frames. Considering the low resolution of far field incident light (NA ~0.2), the sub-diffraction changes of illuminating pattern from the HMM substrate.
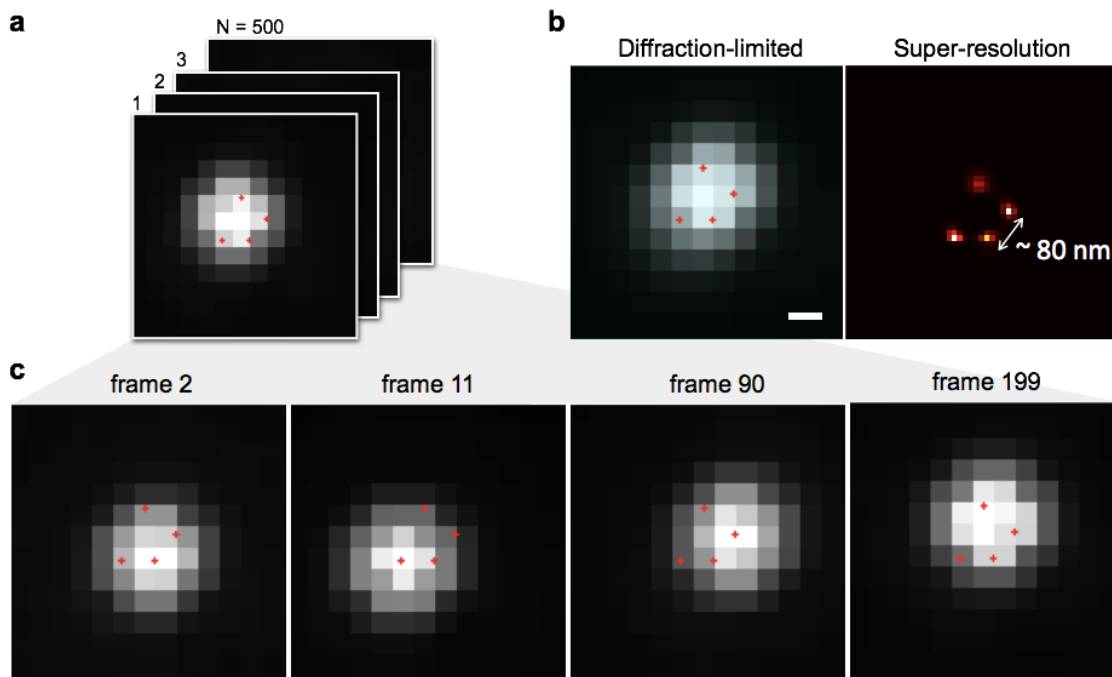
Figure 4.9: Speckle-MAIN raw frames of fluorescent beads. (a) An image stack of fluorescent beads on HMM-coated substrate. Objective lens: Olympus 100X/1.5 oil. Frame rate: 1Hz. Exposure Time: 500 ms. Total frame: 500. (b) Diffraction-limited image and super-resolution image after reconstruction. Locations of reconstructed beads are marked in those raw frames. Diffraction-limited image is computed by averaging all 500 frames. Scale Bar: 100 nm. (c) Four selected frames indicate a sub-diffraction changes of illumination pattern.

4.6.2 Widefield super resolution image

Structured illumination usually can get a super-resolution from a limited number of sub-frames (9-18 frames). Speckle-based blind-SIM, however, lacking the knowledge about exact illumination patterns, requires more frames. Figure 4.6 shows super-resolution imaging from 80 sub-frames and a detection NA of 0.8. Two attached fluorescent beads with ~60 nm spacing is reconstructed and proved by scanning electron microscope (SEM). A single bead in the same image, shows a FWHM of 56 nm after reconstruction. In this dataset, illuminating wavelength is scanned (from 450 nm to 480 nm, step: 10 nm) as well as the incident electrical field to generate distinct speckle patterns from the HMM-coated substrate.

Figure 4.7 presents super-resolution image of a more complex object at a wide field of view (14 um x 14 um). The object is made by drop-casting of dense quantum dot emitting at 605 nm. The quantum dot forms certain nanostructures on top of HMM-coated substrate (figure 6 c,d). Super-resolution image reconstructed from 140 sub-frames reveal many details that cannot be observed by diffraction-limited images. In principle, speckle-MAIN will have a field of view (FOV) as wide as epi-fluorescent microscope, which is limited by the magnification and sensor sizes (CCD or CMOS). However, each reconstructed image will have its size limited by the memory of GPU. A FOV of 14 um x 14 um is achievable in this specific case for a single reconstruction.

The experiment set up for figure 4.6 and figure 4.7 are similar to that of figure 4.5. The difference is that a super-continuum laser (NKT Photonics, extreme) is coupled to an inverted microscope via free space. The laser beam hits on a diffuser first and then is

collected and focused to the sample by the condenser lens. An additional 4X magnification

is used at image plane. The images are acquired by a EMCCD (Andor iXon 897)
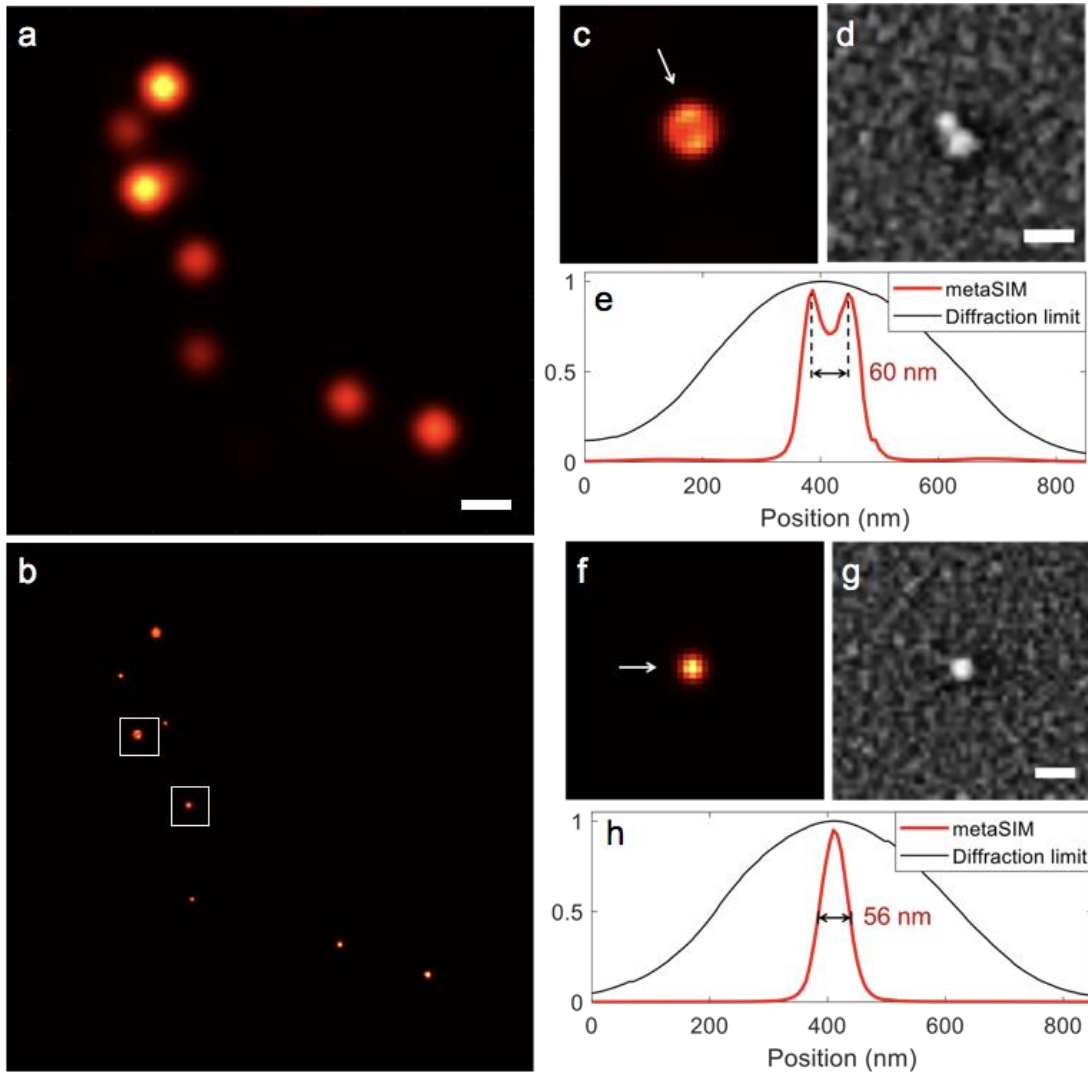
Figure 4.10: Super-resolution image of fluorspheres with 0.8 NA and 80 sub-frames. (a) Diffraction-limit Image. scale bar: 600 nm. Objective lens: Zeiss 50X/0.8. (b) Reconstructed Image. Number of raw camera frames: 80; Illumination Wavelength: 450 nm - 480 nm. Step: 10 nm; Bandwidth: 10 nm. For Each wavelength channel, 20 frames are acquired by changing the scrambled incident optical field. (c,f) zoom in images of (b) at indicated location. (d,g) SEM images of fluospheres at indicated locations. Scale Bar: 100 nm. (e,h) Cross-section of image (c,f) along indicated direction.
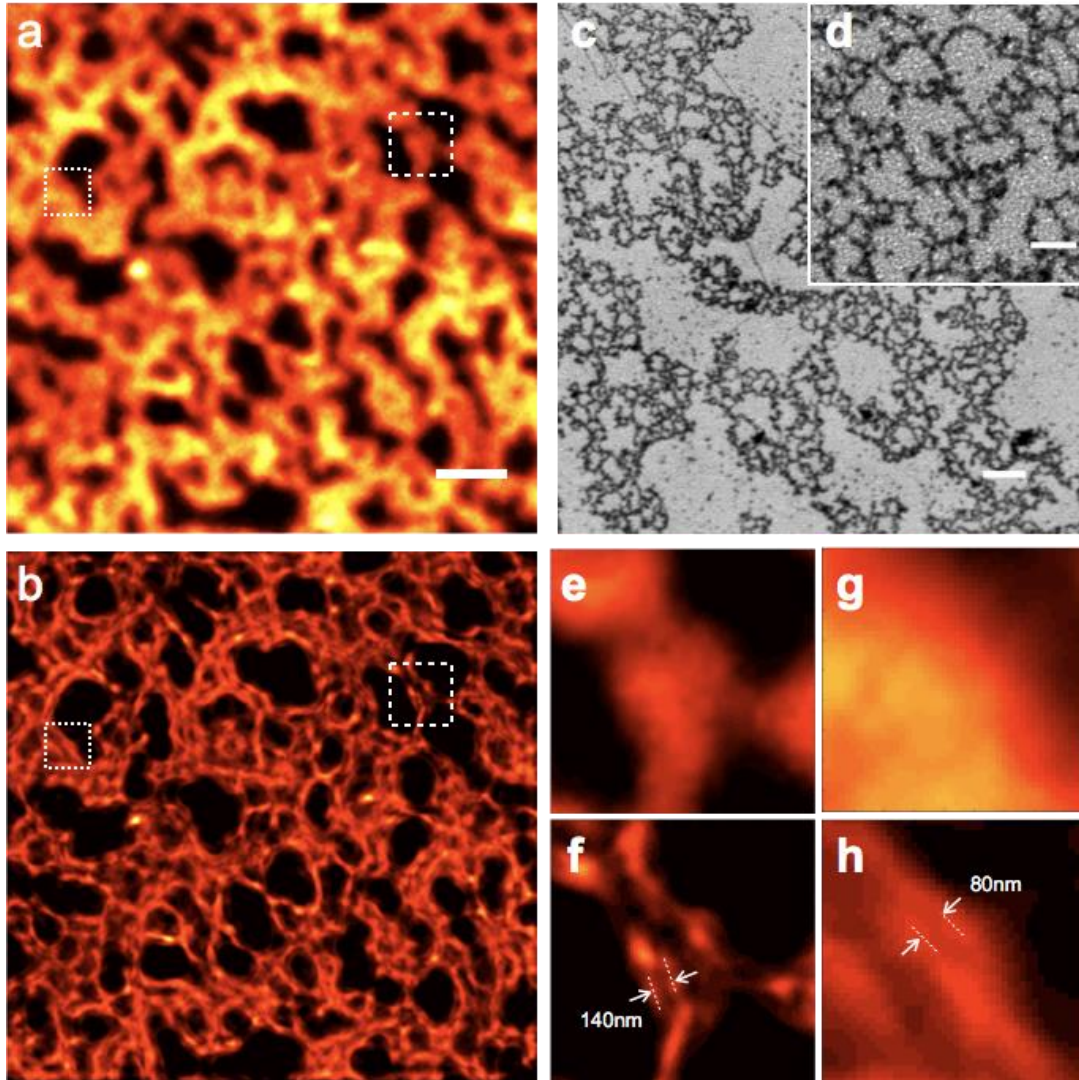
Figure 4.11: Widefield super-resolution image of Qdot 605. (a) Diffraction-limited image. Scale bar: 2 um. FOV: 14 um x 14 um. Objective Lens: 50X/0.8. (b) Reconstructed Image. Number of raw camera frames: 140; Illumination Wavelength: 460 nm - 520 nm. Step: 10 nm; Bandwidth: 10 nm. For Each wavelength channel, 20 frames are acquired by changing the scrambled incident optical field. (c,d) Structure formed by dropcasting Qdot 605 under SEM. Scale bar: 500 nm (c). 250 nm (d). (e,g) Zoom in image of diffraction-limited image and super-resolution image at indicated location (dash), respectively. (f,h) Zoom in image of diffraction-limit image and super-resolution image at indicated location (solid), respectively.

4.7 Discussion

In general, we demonstrate speckle-MAIN, a robust, low-cost on-surface super-resolution method down to 56 nm. The microscope set up is much simplified compared to other super-resolution techniques. The experiment can be conducted under conventional epi-fluorescent microscope, with a HMM-coated substrate and a multi-mode fiber for illumination. Compared to SIM (especially TIRF-based SIM), it greatly extends the resolution to $\sim\lambda/9$ (for 500 nm emission), with a relative low NA objective lens with the cost of increased number of measurements (from 10 to a few hundreds). Compared to localization techniques like PALM/STORM, speckle-MAIN, like other structured illumination-based technology, has low incident power, less number of frames, while MAIN remaining its capability of resolve 60 nm resolution. The HMM-coated substrate has transmission of is 10% at 488 nm and 30% at 405 nm, which can be compensated by increasing illumination power.

The resolution of speckle-MAIN is still limited by the metamaterial itself, i.e. the unit pair size of the Ag-SiO$_2$ multilayer. Therefore, a breakthrough in HMM, such as making epitaxial growth of silver-based multilayer that has much smaller unit pair size, will improve the resolution of speckles.

Chapter 4, in part, is currently being prepared for submission for publication of the material. Q. Ma, L. Khorashad, J. Zhao, Z. Liu. "Metamaterial-assisted speckle illumination microscope". The dissertation author was the first author of this paper.

Chapter 5

Summary and Future Directions

In previous chapters, a novel super-resolution imaging approach, hyperbolic metamaterial (HMM) assisted illumination microscope, is demonstrated both theoretically and experimentally. The approach can be classified into MAIN and Speckle-MAIN, according to the methods of generating illumination patterns. MAIN uses well-designed nanostructures such as nanoholes and nanoslits to generate illumination patterns and scan those patterns by tuning wavelength. The illumination of MAIN can be predicted and/or measured. Speckle-MAIN, on the other hand, uses the imperfection of a multilayer HMM to generate random illumination patterns that are unknown during experiment. Both MAIN and Speckle-MAIN, benefiting from the wide spatial frequency bandwidth of a HMM, projects deep sub-wavelength illuminations.

This chapter summarize some key specifications of MAIN/Speckle-MAIN and discuss several future directions.

5.1 Resolution

MAIN gains resolution from the ultrahigh resolution illumination patterns of a HMM. Experiment on Speckle-MAIN demonstrates ~50 nm resolution. Extending the spatial frequency that is carried by the HMM will further extend the resolution of MAIN

imaging. The three main factors that affect the resolution of a multilayer HMM are: thickness of a multilayer unit pair, material absorption, and coupling method.

The unit pair and absorption are from material property of a multilayer HMM, determining the capability of a HMM to carry spatial frequency waves. The coupling method, defined by the nanostructures (e.g. nanoslits, nanoholes, or rough interfaces), determines if the resolution capability of a HMM can be fully used. Considering that current nanofabrication techniques are capable to go down to 10 nm scale, much smaller than the smallest beam width in a multilayer HMM in experiment, the methods of extending the maximum spatial frequency wave carried by a HMM should be investigated.

5.1.1 Ag-based multilayer

The effective medium theory breaks down when wavelength is close to the unit pair size of a multilayer HMM, results in a cutoff of its frequency curve shown in Fig.4.1a. The derivation can be found in Ref [39]. For a given multilayer system (for example, Ag-SiO$_2$), the thinner unit pair size, the higher spatial frequency wave it supports.

The unit pair size of a multilayer in experiment, however, is limited by thin film deposition techniques such as electron beam evaporation or sputtering. Noble metal such as Ag or Au, during deposition, will form islands firstly, and then gradually merge those islands into continuous amorphous film. This sets a minimum thickness of the metallic film in a multilayer system. For instance, it is hard make continuous Ag film on glass that has bulky silver material property when its thickness is less than 10 nm [79]. Fortunately, researchers have shown that, deposition of silver on a lattice matched substrate such as

83

MgO can make ultrathin epitaxial film [80,81], which opens potential of making Ag-MgO multilayer HMM that has atomic-level unit pair size.

In addition to make Ag layer thinner, replacing the low-index dielectric (SiO_2) to high-index dielectric such as TiO_2 can enlarge the bandwidth of spatial frequency. This is because the propagating wave inside a multilayer HMM, termed propagating polaritons, is a result of coupling between surface plasmon waves of adjacent metal-dielectric interfaces. The coupling is through evanescent wave so that a high index dielectric, in which high-k evanescent wave decays slower than low-index dielectric, will improve the coupling and hence, improve the bandwidth of spatial frequency.

To foresee the improvement from either reducing unit pair size or increasing refractive index of dielectric layer, figure 5.1 compares the Ag-SiO_2 multilayer used in experiment to the Ag-MgO and Ag-TiO_2 material system that can be developed in the future.

5.1.2 Non-Ag-based multilayer

Other non-silver-based multilayer system is capable to have very small unit pair sizes. For instance, Au-Si or Au-SiO_2 multilayer [82,83] can generally be thinner than Ag-based ones. TiN-Al_2O_3 multilayer can make its unit pair size to atomic level [69]. These multilayer systems can have a hyperbolic region from wavelength 600 nm or above. However, the metallic losses of Au and TiN is a dominant factor that limits the resolution, making them not comparable with Ag-based multilayers approaches.
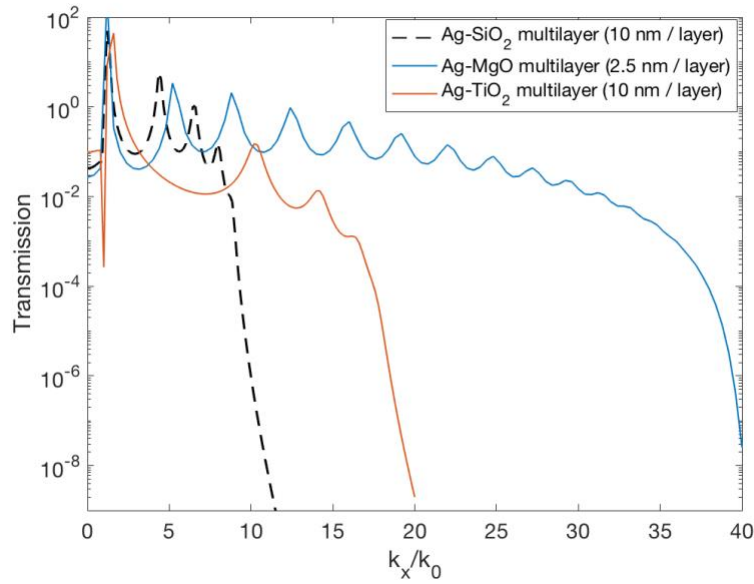
Figure 5.1: Transmission curve versus normalized spatial frequency. Ag-SiO$_2$ multilayer consists of 5 pairs of 10 nm Ag and 10 nm SiO$_2$, wavelength: 500 nm; Ag-MgO multilayer consists of 20 pairs of 2.5 nm Ag and 2.5 nm MgO, wavelength: 500 nm; Ag-TiO$_2$ multilayer consists of 5 pairs of 10 nm Ag and 10 nm TiO$_2$, wavelength: 532 nm. The calculation is done through transfer matrix method. The peaks shown in the plot comes from the multiple reflections from the metal-dielectric interfaces.

5.2 Speed

MAIN/Speckle-MAIN have inherent advantages from SIM and will have a great potential in high spatiotemporal resolution surface imaging. Unlike localization-based microscope or point-scanning STED microscope, MAIN, by well-designing the illumination patterns, needs a minimum number of camera frames to reconstruct a widefield super-resolution imaging. Based on information capacity, a 250-nm diffraction-limited system with an imaging resolution of 25 nm only requires $(250/25)^2 = 100$ frames.

Speckle-MAIN, by using unknown illumination patterns, generally requires more camera frames for a super-resolution imaging. This is because it uses a statistical constraint

that all illumination patterns add up to uniform. However, we've also shown that by applying sparsity constraint on the object, it is still capable to reconstruct super-resolution image from only 80 frames.

5.3 Depth of penetration

MAIN/Speckle-MAIN is a surface image technique. The spatial frequency content of illumination pattern, that is beyond the diffraction limit, decays exponentially in the air. As a result, the resolution of illumination pattern decreases when the plane of interest moves away from the HMM surface. The decay rate of different spatial frequency wave can be estimated by following equation:

$$H = e^{-z\sqrt{k_x^2+k_y^2-k_0^2}} \approx e^{-z\sqrt{k_x^2+k_y^2}}, \qquad (5.1)$$

where z is the distance away from the HMM, k_0 is the wavevector in the air, k_x, k_y are the spatial frequency contents that are much larger than k_0, From the equation, for spatial frequency 1/z0 nm^{-1}, its amplitude decays to $1/e$ when it is z0 nm away from the HMM surface. Thus, the image depth of MAIN can be approximated by the resolution of the reconstructed image.

5.4 Enhancing spontaneous emission

Hyperbolic metamaterials (HMMs), as well as other plasmonic nanostructures, have been extensively used to manipulate the spontaneous light emission rate of molecules

and their radiative efficiency. MAIN, by using HMMs for illumination, will inherently have such enhanced spontaneous emission.

When an emitter is brought close to a HMM, there are three channels to release its energy: radiative emission, non-radiative decay, and plasmonic modes. The plasmonic modes can dominate other modes and greatly enhance the lifespan of a fluorescent molecule. In Ref [84], about 1000-fold increase of harvested photons are reported by making a fluorescent molecule close to plasmonic nano-antenna.

The plasmonic modes, however, are not necessarily to be radiative. Therefore, an outcoupling mechanism is necessary to extract energy from the non-radiative plasmonic modes. Examples of this can be found at Ref [36]. By integrating outcoupling mechanism into HMM, MAIN can be a super-resolution imaging platform that also has elongated lifetime of fluorescent molecules.

5.5 Summary

In this dissertation, we demonstrate MAIN/Speckle-MAIN, which uses a HMM-assisted illumination for structured illumination microscope. Gaining resolution from its metamaterial-shaped illumination, imaging resolution down to 50 nm has been experimentally demonstrated. MAIN is free of selecting fluorescent dyes and is capable to work under low illumination intensity which is beneficial for addressing photobleaching/phototoxicity problem.

Reference

[1]   J. W. Goodman, Opt. Eng. 491 (2004).

[2]   D. B. Murphy and M. W. Davidson, *Fundamentals of Light Microscopy and Electronic Imaging: Second Edition* (2012).

[3]   A. M. Sydor, K. J. Czymmek, E. M. Puchner, and V. Mennella, Trends Cell Biol. **25**, 730 (2016).

[4]   S. J. Sahl, S. W. Hell, and S. Jakobs, Nat Rev Mol Cell Biol **advance on**, (2017).

[5]   S. W. Hell and J. Wichmann, Opt. Lett. **19**, 780 (1994).

[6]   V. Westphal, S. O. Rizzoli, M. A. Lauterbach, D. Kamin, R. Jahn, and S. W. Hell, Science. **320**, 246 (2008).

[7]   T. A. Klar and S. W. Hell, Opt. Lett. **24**, 954 (1999).

[8]   G. Patterson, M. Davidson, S. Manley, and J. Lippincott-Schwartz, Annu. Rev. Phys. Chem. **61**, 345 (2010).

[9]   M. J. Rust, M. Bates, and X. Zhuang, Nat. Methods **3**, 793 (2006).

[10]   A. Sharonov and R. M. Hochstrasser, Proc. Natl. Acad. Sci. U. S. A. **103**, 18911 (2006).

[11]   E. Betzig, G. H. Patterson, R. Sougrat, O. W. Lindwasser, S. Olenych, J. S. Bonifacino, M. W. Davidson, J. Lippincott-Schwartz, and H. F. Hess, Science **313**, 1642 (2006).

[12]   M. G. L. Gustafsson, J. Microsc. **198**, 82 (2000).

[13]   M. G. L. Gustafsson, Proc. Natl. Acad. Sci. **102**, 13081 (2005).

[14]   D. Li, L. Shao, B.-C. Chen, X. Zhang, M. Zhang, B. Moses, D. E. Milkie, J. R. Beach, J. A. Hammer, M. Pasham, T. Kirchhausen, M. A. Baird, M. W. Davidson, P. Xu, and E. Betzig, Science. **349**, aab3500 (2015).

[15]   L. Schermelleh, P. M. Carlton, S. Haase, L. Shao, L. Winoto, P. Kner, B. Burke, M. C. Cardoso, D. A. Agard, M. G. L. Gustafsson, H. Leonhardt, and J. W. Sedat, Science. **320**, 1332 (2008).

[16]   S. Jia, J. C. Vaughan, and X. Zhuang, Nat. Photonics **8**, 302 (2014).

[17]   B. Huang, S. A. Jones, B. Brandenburg, and X. Zhuang, Nat. Methods **5**, 1047 (2008).

[18]   U. Endesfelder and M. Heilemann, Methods Mol. Biol. **1251**, 263 (2014).

[19]   S. T. Hess, T. P. K. Girirajan, and M. D. Mason, Biophys. J. **91**, 4258 (2006).

[20]   F. Balzarotti, Y. Eilers, K. C. Gwosch, A. H. Gynnå, V. Westphal, F. D. Stefani, J. Elf, and S. W. Hell, Science. **355**, 606 (2017).

[21]   M. Shaw, L. Zajiczek, and K. O'Holleran, Methods **88**, 11 (2015).

[22]   F. Ströhl and C. F. Kaminski, Optica **3**, 667 (2016).

[23]   F. Wei and Z. Liu, Nano Lett. **10**, 2531 (2010).

[24]   F. Wei, D. Lu, H. Shen, W. Wan, J. L. Ponsetto, E. Huang, and Z. Liu, Nano Lett. **14**, 4634 (2014).

[25]   A. G. York, S. H. Parekh, D. D. Nogare, R. S. Fischer, K. Temprine, M. Mione, A. B. Chitnis, C. A. Combs, and H. Shroff, Nat. Methods **9**, 749 (2012).

[26]   E. Mudry, K. Belkebir, J. Girard, J. Savatier, E. Le Moal, C. Nicoletti, M. Allain, and A. Sentenac, Nat. Photonics **6**, 312 (2012).

[27]   A. Poddubny, I. Iorsh, P. Belov, and Y. Kivshar, Nat. Photonics **7**, 948 (2013).

[28]   L. Ferrari, C. Wu, D. Lepage, X. Zhang, and Z. Liu, Prog. Quantum Electron. **40**, 1 (2015).

[29]   Z. Jacob, L. V. Alekseyev, and E. Narimanov, Opt. Express **14**, 8247 (2006).

[30]   D. Lu and Z. Liu, Nat. Commun. **3**, 1205 (2012).

[31]   S. Thongrattanasiri and V. A. Podolskiy, Opt. Lett. **34**, 890 (2009).

[32]   S. Ishii, A. V. Kildishev, E. Narimanov, V. M. Shalaev, and V. P. Drachev, Laser Photonics Rev. **7**, 265 (2013).

[33]   Y. Xiong, Z. Liu, and X. Zhang, Appl. Phys. Lett. **94**, (2009).

[34]   Z. Jacob, J. Y. Kim, G. V. Naik, A. Boltasseva, E. E. Narimanov, and V. M. Shalaev, Appl. Phys. B Lasers Opt. **100**, 215 (2010).

[35]   M. A. Noginov, H. Li, Y. A. Barnakov, D. Dryden, G. Nataraj, G. Zhu, C. E. Bonner, M. Mayy, Z. Jacob, and E. E. Narimanov, Opt. Lett. **35**, 1863 (2010).

[36]   D. Lu, J. J. Kan, E. E. Fullerton, and Z. Liu, Nat. Nanotechnol. **9**, 48 (2014).

[37] C. L. Cortes, W. Newman, S. Molesky, and Z. Jacob, J. Opt. (United Kingdom) **14**, (2012).

[38] D. J. Bergman, Phys. Rep. **43**, 377 (1978).

[39] B. Wood, J. B. Pendry, and D. P. Tsai, Phys. Rev. B **74**, 115116 (2006).

[40] M. A. Noginov, Y. A. Barnakov, G. Zhu, T. Tumkur, H. Li, and E. E. Narimanov, Appl. Phys. Lett. **94**, (2009).

[41] J. Yao, Z. Liu, Y. Liu, Y. Wang, C. Sun, G. Bartal, A. M. Stacy, and X. Zhang, Science. **321**, 930 (2008).

[42] J. D. Caldwell, A. V. Kretinin, Y. Chen, V. Giannini, M. M. Fogler, Y. Francescato, C. T. Ellis, J. G. Tischler, C. R. Woods, A. J. Giles, M. Hong, K. Watanabe, T. Taniguchi, S. A. Maier, and K. S. Novoselov, Nat. Commun. **5**, (2014).

[43] S. Dai, Q. Ma, M. K. Liu, T. Andersen, Z. Fei, M. D. Goldflam, M. Wagner, K. Watanabe, T. Taniguchi, M. Thiemens, F. Keilmann, G. C. A. M. Janssen, S. E. Zhu, P. Jarillo-Herrero, M. M. Fogler, and D. N. Basov, Nat. Nanotechnol. **10**, 682 (2015).

[44] J. B. Pendry, Phys. Rev. Lett. **85**, 3966 (2000).

[45] N. Fang, H. Lee, C. Sun, and X. Zhang, Science. **308**, 534 LP (2005).

[46] T. Taubner, D. Korobkin, Y. Urzhumov, G. Shvets, and R. Hillenbrand, Science. **313**, 1595 (2006).

[47] Z. Liu, S. Durant, H. Lee, Y. Pikus, N. Fang, Y. Xiong, C. Sun, and X. Zhang, Nano Lett. **7**, 403 (2007).

[48] Z. Liu, H. Lee, Y. Xiong, C. Sun, and X. Zhang, Science. **315**, 1686 (2007).

[49] J. Rho, Z. Ye, Y. Xiong, X. Yin, Z. Liu, H. Choi, G. Bartal, and X. Zhang, Nat. Commun. **1**, 143 (2010).

[50] I. I. Smolyaninov, Y. J. Hung, and C. C. Davis, Science. **315**, 1699 (2007).

[51] C. Ma, J. Nanophotonics **5**, 51604 (2011).

[52] M. Khorasaninejad, W. T. Chen, R. C. Devlin, J. Oh, A. Y. Zhu, and F. Capasso, Science. **352**, 1190 LP (2016).

[53] A. V. Kildishev and V. M. Shalaev, Opt. Lett. **33**, 43 (2008).

[54] S. Han, Y. Xiong, D. Genov, Z. Liu, G. Bartal, and X. Zhang, Nano Lett. **8**, 4243 (2008).

[55] J. L. Ponsetto, F. Wei, and Z. Liu, Nanoscale **6**, 5807 (2014).

[56] J. L. Ponsetto, A. Bezryadina, F. Wei, K. Onishi, H. Shen, E. Huang, L. Ferrari, Q. Ma, Y. Zou, and Z. Liu, ACS Nano **11**, 5344 (2017).

[57] E. Narimanov, ACS Photonics **3**, 1090 (2016).

[58] E. Khan and E. E. Narimanov, Appl. Phys. Lett. **111**, (2017).

[59] M. F. Duarte, M. A. Davenport, D. Takhar, J. N. Laska, K. F. Kelly, and R. G. Baraniuk, IEEE Signal Process. Mag. **25**, 83 (2008).

[60] E. J. Candes and M. B. Wakin, IEEE Signal Process. Mag. **25**, 21 (2008).

[61] J. Romberg, IEEE Signal Process. Mag. **25**, 14 (2008).

[62] W. L. Chan, K. Charan, D. Takhar, K. F. Kelly, R. G. Baraniuk, and D. M. Mittleman, Appl. Phys. Lett. **93**, 121105 (2008).

[63] E. Huang, Q. Ma, and Z. Liu, Sci. Rep. **6**, 25240 (2016).

[64] J. Hunt, T. Driscoll, A. Mrozack, G. Lipworth, M. Reynolds, D. Brady, and D. R. Smith, Science. **339**, 310 (2013).

[65] S. B. Kwangmoo Koh, Seung-Jean Kim, J. Mach. Learn. Res. **8**, 1519 (2007).

[66] Y. Shechtman, Y. C. Eldar, A. Szameit, and M. Segev, Opt. Express **19**, 14807 (2011).

[67] A. Szameit, Y. Shechtman, E. Osherovich, E. Bullkich, P. Sidorenko, H. Dana, S. Steiner, E. B. Kley, S. Gazit, T. Cohen-Hyams, S. Shoham, M. Zibulevsky, I. Yavneh, Y. C. Eldar, O. Cohen, and M. Segev, Nat. Mater. **11**, 455 (2012).

[68] D. M. SHOTTON, J. Cell Sci. **94**, 175 (1989).

[69] B. Saha, G. V Naik, S. Saber, C. Akatay, E. A. Stach, V. M. Shalaev, A. Boltasseva, and T. D. Sands, Phys. Rev. B **90**, 125420 (2014).

[70] M. Hofmann, C. Eggeling, S. Jakobs, and S. W. Hell, Proc. Natl. Acad. Sci. United States Am. **102**, 17565 (2005).

[71] B.-C. Chen, W. R. Legant, K. Wang, L. Shao, D. E. Milkie, M. W. Davidson, C. Janetopoulos, X. S. Wu, J. A. Hammer, Z. Liu, B. P. English, Y. Mimori-Kiyosue, D. P. Romero, A. T. Ritter, J. Lippincott-Schwartz, L. Fritz-Laylin, R. D. Mullins, D. M. Mitchell, J. N. Bembenek, A.-C. Reymann, R. Bohme, S. W. Grill, J. T. Wang, G. Seydoux, U. S. Tulu, D. P. Kiehart, and E. Betzig, Science. **346**, 1257998 (2014).

[72] L. J. Young, F. Ströhl, and C. F. Kaminski, J. Vis. Exp. (2016).

[73] Y. Blau, D. Shterman, G. Bartal, and B. Gjonaj, Opt. Lett. Vol. 41, Issue 15, Pp. 3455-3458 **41**, 3455 (2016).

[74] H. Shen, D. Lu, B. VanSaders, J. J. Kan, H. Xu, E. E. Fullerton, and Z. Liu, Phys. Rev. X **5**, 21021 (2015).

[75] P. B. Johnson and R. W. Christy, Phys. Rev. B **6**, 4370 (1972).

[76] N. Garcia and E. Stoll, Phys. Rev. Lett. **52**, 1798 (1984).

[77] T. W. Murray, M. Haltmeier, T. Berer, E. Leiss-Holzinger, and P. Burgholzer, Optica **4**, 17 (2017).

[78] A. Beck and M. Teboulle, SIAM J. Imaging Sci. **2**, 183 (2009).

[79] J. Gong, R. Dai, Z. Wang, and Z. Zhang, Sci. Rep. **5**, (2015).

[80] D. Velázquez, R. Seibert, Z. Yusof, J. Terry, and L. Spentzouris, in *6th Int. Part. Accel. Conf. IPAC 2015* (2015).

[81] P. W. Palmberg, T. N. Rhodin, and C. J. Todd, Appl. Phys. Lett. **11**, 33 (1967).

[82] H. Qian, Y. Xiao, D. Lepage, and Z. Liu, Cleo 2015 **1**, SM1G.7 (2015).

[83] H. Qian, Y. Xiao, and Z. Liu, Nat. Commun. **7**, (2016).

[84] H. Cang, Y. Liu, Y. Wang, X. Yin, and X. Zhang, Nano Lett. **13**, 5949 (2013).